Published in final edited form as:
Nature. 2014 September 4; 513(7516): 90–94. doi:10.1038/nature13608.

RIPK1 maintains epithelial homeostasis by inhibiting apoptosis and necroptosis

Marius Dannappel[1,*], **Katerina Vlantis**[1,*], **Snehlata Kumari**[1,*], **Apostolos Polykratis**[1,*], **Chun Kim**[1], **Laurens Wachsmuth**[1], **Christina Eftychi**[1], **Juan Lin**[1], **Teresa Corona**[1], **Nicole Hermance**[2], **Matija Zelic**[2], **Petra Kirsch**[3], **Marijana Basic**[4], **Andre Bleich**[4], **Michelle Kelliher**[2,§], and **Manolis Pasparakis**[1,§]

[1]Institute for Genetics, Centre for Molecular Medicine (CMMC), and Cologne Excellence Cluster on Cellular Stress Responses in Aging-Associated Diseases (CECAD), University of Cologne, 50931 Cologne, Germany.

[2]Department of Cancer Biology, University of Massachusetts Medical School, Worcester, Massachusetts 01605, USA.

[3]Tierforschungszentrum, University of Ulm, Albert-Einstein-Allee 11, D-89081 Ulm, Germany.

[4]Institute for Laboratory Animal Science, Hannover Medical School, D-30625 Hannover, Germany.

Abstract

Necroptosis has emerged as an important pathway of programmed cell death in embryonic development, tissue homeostasis, immunity and inflammation[1–8]. RIPK1 is implicated in inflammatory and cell death signalling[9–13] and its kinase activity is believed to drive RIPK3-mediated necroptosis[14,15]. Here we show that kinase-independent scaffolding RIPK1 functions regulate homeostasis and prevent inflammation in barrier tissues by inhibiting epithelial cell apoptosis and necroptosis. Intestinal epithelial cell (IEC)-specific RIPK1 knockout caused IEC apoptosis, villus atrophy, loss of goblet and Paneth cells and premature death in mice. This pathology developed independently of the microbiota and of MyD88 signalling but was partly rescued by TNFR1 (also known as TNFRSF1A) deficiency. Epithelial FADD ablation inhibited IEC apoptosis and prevented the premature death of mice with IEC-specific RIPK1 knockout.

Correspondence and requests for materials should be addressed to M.P. (pasparakis@uni-koeln.de).
*These authors contributed equally to this work.
§These authors jointly supervised this work.

Online Content Methods, along with any additional Extended Data display items and Source Data, are available in the online version of the paper; references unique to these sections appear only in the online paper.

Author Contributions M.D. together with K.V. performed and analysed the experiments related to the intestine and S.K. performed and analysed the experiments related to the skin. N.H. and M.K. designed and generated the targeting constructs for the *Ripk1*$^{fl/fl}$ and *Ripk1*$^{D138N/D138N}$ mice. A.P. performed the gene targeting in embryonic stem cells and generated the *Ripk1*$^{fl/fl}$, *Ripk1*$^{D138N/D138N}$ and *Trif*$^{fl/fl}$ mice. M.Z. contributed to the analysis of intestines from *Ripk1*$^{-/-}$ neonates. C.K. and J.L. performed biochemical analysis of RIPK1-deficient MEFs, IECs and keratinocytes. C.E. performed FACS analysis of intestinal immune cells. T.C. performed qRT–PCR analysis. L.W. designed and tested the short guiding RNAs for CRISPR/Cas9-mediated targeting of *Mlkl*. P.K., M.B. and A.B. generated germ-free RIPK1$^{IEC\text{-}KO}$ mice. M.P. coordinated the project and together with K.V., M.D. and S.K. wrote the paper.

The authors declare no competing financial interests. Readers are welcome to comment on the online version of the paper.

However, mice lacking both RIPK1 and FADD in IECs displayed RIPK3-dependent IEC necroptosis, Paneth cell loss and focal erosive inflammatory lesions in the colon. Moreover, a RIPK1 kinase inactive knock-in delayed but did not prevent inflammation caused by FADD deficiency in IECs or keratinocytes, showing that RIPK3-dependent necroptosis of FADD-deficient epithelial cells only partly requires RIPK1 kinase activity. Epidermis-specific RIPK1 knockout triggered keratinocyte apoptosis and necroptosis and caused severe skin inflammation that was prevented by RIPK3 but not FADD deficiency. These findings revealed that RIPK1 inhibits RIPK3-mediated necroptosis in keratinocytes *in vivo* and identified necroptosis as a more potent trigger of inflammation compared with apoptosis. Therefore, RIPK1 is a master regulator of epithelial cell survival, homeostasis and inflammation in the intestine and the skin.

Mice lacking RIPK1 die perinatally, exhibiting apoptosis in multiple tissues including the intestine[9] (Extended Data Fig. 1a). We generated mice with IEC-specific knockout of RIPK1 (RIPK1$^{IEC\text{-}KO}$) (Fig. 1a and Extended Data Fig. 1b–d) and found that they showed reduced body weight and died within the first 4 weeks of life (Fig. 1b, c). Intestinal sections from 3-week-old RIPK1$^{IEC\text{-}KO}$ mice revealed pronounced villus atrophy and Paneth cell loss in the ileum, as well as reduced numbers of goblet cells and differentiated enterocytes, crypt elongation and IEC hyperproliferation in both the ileum and colon (Fig. 1d and Extended Data Fig. 1e, f). RIPK1$^{IEC\text{-}KO}$ intestines contained highly increased numbers of cleaved caspase-3-positive (CC3^{+}) apoptotic IECs, but did not show signs of epithelial erosion, suggesting that the epithelial barrier remained largely intact (Fig. 1d and Extended Data Fig. 1e, f). Messenger RNA levels of *Tnf*, *Il1b*, *Ccl5* and *Cxcl1* and leukocyte numbers were moderately increased in the ileum and colon of RIPK1$^{IEC\text{-}KO}$ mice (Fig. 1e, f and Extended Data Fig. 2), indicating the presence of a mild inflammatory response. Newborn RIPK1$^{IEC\text{-}KO}$ mice showed only a few apoptotic IECs, while 7-day-old mice showed increased numbers of apoptotic IECs, loss of goblet cells, elongated hyperproliferative crypts and increased immune cell infiltration concomitant with moderately increased expression of tumour necrosis factor (TNF) and interleukin (IL)-1β (Extended Data Fig. 3). Tamoxifen-inducible ablation of RIPK1 in IECs of adult mice (RIPK1$^{tamIEC\text{-}KO}$) caused rapid weight loss and death of the animals (Extended Data Fig. 4a–d) due to extensive IEC apoptosis resulting in severe intestinal pathology (Extended Data Fig. 4e–i). Collectively, these results revealed that epithelial-cell-intrinsic RIPK1 is essential for IEC survival and the maintenance of intestinal tissue structure and homeostasis.

The luminal microbiota regulates intestinal homeostasis and contributes to inflammation both in human inflammatory bowel disease and in mouse models[16,17]. Antibiotic treatment briefly delayed but did not prevent severe intestinal pathology, weight loss and death of mice with inducible or constitutive IEC-specific RIPK1 knockout (Extended Data Fig. 4c–e, j–l). Moreover, RIPK1$^{IEC\text{-}KO}$ mice raised under germ-free conditions developed similar intestinal pathology, although some of the mice survived up to the age of 5 weeks, indicating that the microbiota contributes to disease severity (Fig. 1g–j). In addition, MyD88 deficiency did not prevent intestinal pathology in RIPK1$^{IEC\text{-}KO}$ mice (Fig. 2a, b, d and Extended Data Fig. 5a–c). Therefore, epithelial cell death and intestinal pathology in RIPK1$^{IEC\text{-}KO}$ mice develop independently of the microbiota and of MyD88-dependent TLR signalling. RIPK1$^{IEC\text{-}KO}$/*Tnfr1*$^{-/-}$ mice were partially protected from severe wasting, with

approximately 50% of the mice surviving to at least 3 months of age, and showed reduced IEC apoptosis and ameliorated intestinal pathology (Fig. 2a–e and Extended Data Fig. 5a–c). Thus, IEC death and intestinal pathology in RIPK1^{IEC-KO} mice is induced mainly by TNFR1 signalling but TNFR1-independent pathways also contribute.

Epithelial FADD deficiency inhibited IEC apoptosis and villus atrophy and prevented the severe wasting and premature death of RIPK1^{IEC-KO} mice (Fig. 2f–h), suggesting an important pathogenic role of FADD-dependent apoptosis. However, RIPK1^{IEC-KO}/FADD^{IEC-KO} intestines contained increased numbers of CC3^{-} dying IECs and showed Paneth cell loss in the ileum and signs of colitis affecting primarily the distal colon (Fig. 2f, i, j and Extended Data Fig. 6). In contrast with RIPK1^{IEC-KO} mice, in which the distal colon was only mildly affected and that did not show epithelial erosions (0 of 18 mice analysed), histological examination of Swiss roll sections revealed focal epithelial erosions in the distal colon of RIPK1^{IEC-KO}/FADD^{IEC-KO} mice (8 of 14 mice) and RIPK1^{IEC-KO} mice with heterozygous epithelial FADD deficiency (FADD$^{hetIEC-KO}$) (5 of 6 mice) at the age of 3 weeks (Extended Data Fig. 6). Adult RIPK1^{IEC-KO}/FADD^{IEC-KO} mice displayed villus shortening, loss of goblet and Paneth cells and crypt elongation in the small intestine, as well as focal inflammatory erosive lesions and crypt abscess formation in the distal colon in 5 of 7 mice examined (Extended Data Fig. 7a). Therefore, although epithelial FADD deficiency strongly reduced the number of apoptotic epithelial cells and prevented wasting and premature death of RIPK1^{IEC-KO} mice, it did not normalize but rather altered their intestinal pathology, with RIPK1^{IEC-KO}/FADD^{IEC-KO} animals resembling the phenotype of FADD^{IEC-KO} mice[5].

We reasoned that RIPK3-dependent necroptosis could induce the death of IECs in RIPK1^{IEC-KO}/FADD^{IEC-KO} mice, as in FADD^{IEC-KO} mice[5]. Indeed, triple-deficient RIPK1^{IEC-KO}/FADD^{IEC-KO}/*Ripk3*$^{-/-}$ mice did not show macroscopic or histological signs of intestinal pathology, although they displayed slightly increased mRNA levels of *Tnf*, *Il1b*, *Ccl5* and *Il10* in the colon (Fig. 2f–k and Extended Data Figs 5d, e, 6, 7a, b). In contrast, RIPK3 deficiency alone did not prevent wasting, early lethality, IEC apoptosis or intestinal pathology in RIPK1^{IEC-KO} mice (Fig. 2f–j and Extended Data Figs 5d, e, 6, 7b). Therefore, RIPK3-dependent necroptosis does not constitute a primary pathway inducing IEC death and intestinal pathology in RIPK1^{IEC-KO} mice, but becomes functionally important when FADD ablation inhibits apoptosis and sensitizes RIPK1-deficient IECs to necroptosis. These results suggested that RIPK3 induces RIPK1-independent necroptosis in FADD-deficient IECs, which is surprising as RIPK1 kinase activity is considered essential for RIPK3-mediated necroptosis, at least downstream of TNFR1 (refs 14, 15), which is the major driver of epithelial cell necroptosis in the colon of FADD^{IEC-KO} mice[5]. To address specifically the role of RIPK1 kinase activity, we crossed FADD^{IEC-KO} mice with knock-in mice expressing kinase-inactive RIPK1 (RIPK1 (D138N)) and found that lack of RIPK1 kinase activity did not prevent IEC necroptosis and intestinal inflammation in FADD^{IEC-KO} mice (Fig. 2l and Extended Data Fig. 7c, d). Therefore, RIPK1 deficiency or loss of its kinase activity only partly inhibited RIPK3-dependent necroptosis of FADD-deficient IECs, providing genetic evidence that both RIPK1-dependent and RIPK1-independent pathways drive RIPK3-mediated necroptosis and intestinal inflammation in FADD^{IEC-KO} mice.

As shown previously[9,18], RIPK1 deficiency but not loss of its kinase activity partially inhibited TNF-mediated NF-κB activation in mouse embryonic fibroblasts (MEFs) (Extended Data Fig. 8a), suggesting that loss of RIPK1 scaffolding function might trigger epithelial cell apoptosis by inhibiting NF-κB. However, NF-κB inhibition in the intestinal epithelium did not phenocopy the intestinal pathology of RIPK1$^{IEC\text{-}KO}$ mice[19–21]. Moreover, sustained NF-κB activation in RIPK1-deficient epithelial cells by expression of a constitutively active *Ikk2* transgene[22,23] did not prevent IEC death and rather aggravated the intestinal pathology of RIPK1$^{IEC\text{-}KO}$ mice, suggesting that RIPK1 deficiency does not sensitize IECs to apoptosis by inhibiting NF-κB (Extended Data Fig. 8b–d).

RIPK1-deficient IECs did not show reduced mRNA expression of pro-survival genes, but expressed reduced amounts of cIAP1 (also known as BIRC2) and TRAF2 proteins (Fig. 3a, b), suggesting that RIPK1 might control their stability. Indeed, consistent with previous reports[24,25], we found that TNF stimulation induced rapid degradation of TRADD, cIAP1, TRAF2 and c-FLIP (also known as CFLAR), but not of TRAF6, in RIPK1-deficient but not in RIPK1(D138N) primary MEFs (Fig. 3c), suggesting that lack of the RIPK1 scaffolding function triggers degradation of proteins recruited to the TNFR1 signalling complex. We then sought to address whether RIPK1-deficient intestinal epithelial cells show similar responses. However, small intestinal crypts from RIPK1$^{IEC\text{-}KO}$ mice died shortly after isolation and failed to form organoids (data not shown). Nevertheless, tamoxifen-inducible RIPK1 deletion resulted in reduced expression of cIAP1, TRAF2 and c-FLIP proteins and caused rapid organoid death (Fig. 3d–f), suggesting that loss of pro-survival protein expression contributes to death of RIPK1-deficient IECs. Interestingly, TRAF2-deficient mice develop a similar intestinal phenotype and early lethality that was not prevented by antibiotic treatment and was only partially rescued by TNFR1 deficiency, suggesting that loss of TRAF2 could contribute to the intestinal pathology of RIPK1$^{IEC\text{-}KO}$ mice[26].

SMAC (also known as DIABLO) mimetic-compound-mediated cIAP1/2 degradation induced activation of both non-canonical and canonical NF-κB and the expression of TNF and other cytokines[27,28], suggesting that loss of cIAP proteins could trigger the expression of TNF and other cytokines by RIPK1-deficient IECs that could act in an autocrine fashion to induce their death. Indeed, RIPK1-deficient primary IECs showed increased NF-κB activation and expressed elevated levels of TNF, while tamoxifen-inducible deletion of RIPK1 upregulated TNF expression in organoids (Fig. 3g–j). Moreover, intestinal crypts from RIPK1$^{IEC\text{-}KO}$/*Tnfr1*$^{-/-}$ mice did not die rapidly, as did crypts from RIPK1$^{IEC\text{-}KO}$ mice, and although they did not grow as well as control organoids they could be maintained for a short period in culture (Fig. 3k), consistent with a role of autocrine TNF production in triggering the death of RIPK1-deficient IECs. RIPK1/TNFR1 double-deficient organoids were more sensitive to death induced by polyinosinic:polycytidylic acid (poly(I:C)), interferon (IFN)-β and IFN-γ (Fig. 3k), indicating that TIR-domain-containing adapter-inducing interferon-β (TRIF)- and IFN-dependent pathways also contribute to the death of RIPK1-deficient IECs. However, IEC-specific ablation of TRIF did not considerably ameliorate intestinal pathology in RIPK1$^{IEC\text{-}KO}$ mice (Extended Data Fig. 8e–h), suggesting that TRIF-mediated signalling is not a major driver of IEC apoptosis but could contribute in a redundant fashion together with TNFR1 and IFN signalling. Together, these findings suggest that RIPK1 deficiency results in degradation of cIAP proteins and TRAF2,

triggering NF-κB-mediated expression of TNF and other cytokines that act in a partly redundant fashion to induce the death of RIPK1-deficient IECs. The mild upregulation of *Tnf* in the colon of RIPK1$^{IEC\text{-}KO}$/FADD$^{IEC\text{-}KO}$/*Ripk3*$^{-/-}$ mice (Fig. 2k) is compatible with this epithelial cell death independent mechanism inducing *Tnf* expression, which also provides a microbiota-independent trigger of IEC death in RIPK1$^{IEC\text{-}KO}$ mice.

To investigate the function of RIPK1 in the epidermis, we generated mice with keratinocyte-specific RIPK1 deficiency (RIPK1$^{E\text{-}KO}$ mice) (Extended Data Fig. 9a). RIPK1$^{E\text{-}KO}$ mice progressively developed severe inflammatory skin lesions starting at around 1 week of age, characterized by epidermal thickening, increased keratin 14 (K14; also known as KRT14) and reduced K10 expression and upregulation of K6 in the interfollicular epidermis, as well as infiltration of Gr-1-positive cells and increased inflammatory cytokine and chemokine expression (Fig. 4a–c and Extended Data Fig. 9a, b). Histological analysis revealed the presence of CC3^{+} but also CC3^{-} dying keratinocytes, identified by their pyknotic nuclei and eosinophilic cytoplasm in the epidermis of RIPK1$^{E\text{-}KO}$ mice (Fig. 4d and Extended Data Fig. 9d). To address the role of FADD-mediated apoptosis, we generated FADD$^{E\text{-}KO}$/RIPK1$^{E\text{-}KO}$ mice and found that they did not show early postnatal skin inflammation and death, as did FADD$^{E\text{-}KO}$ mice[4], but developed severe inflammatory skin lesions later, similarly to RIPK1$^{E\text{-}KO}$ mice (Fig. 4a–c and Extended Data Fig. 9c, d). Importantly, FADD$^{E\text{-}KO}$/*Ripk1*$^{D138N/D138N}$ mice showed a similar skin phenotype to FADD$^{E\text{-}KO}$/RIPK1$^{E\text{-}KO}$ mice (Fig. 4a, b). Therefore, lack of RIPK1 or its kinase activity delayed but could not prevent keratinocyte necroptosis and inflammation caused by FADD deficiency. Additional deficiency in RIPK3 fully prevented skin inflammation in RIPK1$^{E\text{-}KO}$/FADD$^{E\text{-}KO}$/*Ripk3*$^{-/-}$ mice (Fig. 4a–c and Extended Data Fig. 9e, g), showing that RIPK1-independent RIPK3-dependent keratinocyte necroptosis drives skin inflammation.

Surprisingly, RIPK1$^{E\text{-}KO}$/*Ripk3*$^{-/-}$ mice did not develop skin inflammation and their epidermis contained strongly reduced numbers of CC3^{-} but similar numbers of CC3^{+} keratinocytes compared with RIPK1$^{E\text{-}KO}$ mice (Fig. 4a–d and Extended Data Fig. 9d, e, g), showing that RIPK3-mediated necroptosis of RIPK1-deficient keratinocytes causes the inflammatory skin lesions. CRISPR/Cas9-mediated knockout of MLKL also prevented skin inflammation in RIPK1$^{E\text{-}KO}$ mice, further supporting an essential role of RIPK3/MLKL-dependent necroptosis in this model (Extended Data Fig. 10). Therefore, at least in the context of keratinocyte-specific RIPK1 deficiency, necroptosis of keratinocytes triggers skin inflammation but apoptosis does not, highlighting the different immune regulatory properties of these programmed cell death pathways in a disease-relevant *in vivo* experimental setting. Considering that *Ripk1*$^{D138N/D138N}$ mice did not develop skin lesions (Fig. 4a), these results show that RIPK1 acts through a kinase-independent scaffolding function to restrain RIPK3-mediated necroptosis in keratinocytes and prevent skin inflammation.

RIPK1$^{E\text{-}KO}$/*Tnfr1*$^{-/-}$ mice showed largely normal skin until postnatal day (P)28, but developed patchy inflammatory skin lesions by the age of 7–8 weeks (Fig. 4a–d and Extended Data Fig. 9d, e, g). Therefore, TNFR1 critically contributes but is not the only trigger of keratinocyte necroptosis and inflammation in RIPK1$^{E\text{-}KO}$ mice. Keratinocyte-specific TRIF ablation also mildly ameliorated skin lesion development in RIPK1$^{E\text{-}KO}$ mice

(Fig. 4a, b and Extended Data Fig. 9e). Collectively, these results showed that TNFR1- and TRIF-mediated signalling contribute to RIPK3-dependent keratinocyte necroptosis and skin inflammation in RIPK1$^{E\text{-}KO}$ mice.

cIAP1 was expressed at very low levels at steady state and was undetectable after TNF stimulation in RIPK1-deficient primary keratinocytes (Fig. 4e), similar to our findings in IECs. Moreover, RIPK1-deficient primary keratinocytes were highly sensitive to TNF-induced death that was inhibited by the caspase inhibitor z-VAD-FMK, demonstrating that *in vitro* these cells died primarily by apoptosis and were resistant to necroptosis even though they expressed RIPK3 (Fig. 4f, g). This result is surprising considering that RIPK1 deficiency *in vivo* triggers skin inflammation by sensitizing keratinocytes to RIPK3-dependent necroptosis, and suggests that mechanisms related to keratinocyte differentiation and the *in vivo* tissue context could determine the sensitivity of keratinocytes to apoptosis and necroptosis.

Collectively, our results revealed a novel kinase-independent scaffolding function of RIPK1 as an inhibitor of epithelial cell apoptosis and necroptosis *in vivo* that is essential for the maintenance of physiological tissue homeostasis in the intestine and the skin. The mechanisms determining whether RIPK1 deficiency sensitizes epithelial cells to apoptosis or necroptosis remain unclear and do not seem to depend on differential expression of RIPK3 (Fig. 4g). Our experiments also showed that necroptosis of FADD-deficient IECs and keratinocytes only partly depends on RIPK1 kinase activity, demonstrating that both RIPK1-dependent and -independent pathways drive RIPK3-mediated necroptosis. Therefore, RIPK1 is a central regulator of cell death that has the capacity to either inhibit or induce apoptosis and necroptosis (Fig. 4h). Considering its key role as a molecular hub integrating and decoding multiple ubiquitination (K63, K48, linear) signals to determine cellular responses to stimuli that are derived (for example, lipopolysaccharide, double-stranded RNA) or induced (for example, TNF, IFNs) bymicrobes and are capable of triggering both inflammation and cell death, RIPK1 emerges as a key regulator of immunity and homeostasis in barrier tissues.

Note added in proof: An accompanying paper (Takahashi, N. *et al.*, *Nature* http://dx.doi.org/10.1038/nature13706) reports similar results on the role of RIPK1 in preventing IEC apoptosis, with some differences on the effect of antibiotic treatment and MYD88 deficiency on the intestinal pathology of RIPK1$^{IEC\text{-}KO}$ mice.

METHODS

Mice

Ripk1$^{fl/fl}$, *Ripk1*$^{D138N/D138N}$ (ref. 29), *Trif*$^{fl/fl}$, *Fadd*$^{fl/fl}$ (ref. 30), FADD-IRES-eGFP$^{fl/fl}$ (ref. 4) and *R26-Stop*^{fl}*Ikk2ca*[22] mice expressing a constitutively active *Ikk2* (*Ikk2ca*) transgene were generated by gene targeting in C57BL/6 embryonic stem (ES) cells. FLPe-Deleter[31] mice were used to delete the FRT-flanked neo cassette and Cre-Deleter[32] mice were employed to delete the RIPK1 floxed sequences in the germ line and generate *Ripk1*$^{-/-}$ mice and MEFs. Villin-Cre[33], VillinCreER^{T2} (ref. 34), K14-Cre[35], *Tnfr1*$^{-/-}$ (ref. 36), *Myd88*$^{-/-}$ (ref. 37) and *Ripk3*$^{-/-}$ (ref. 38) mice were backcrossed for at least ten generations into the

C57BL/6 genetic background. Mice were maintained at the SPF animal facilities of the Institute for Genetics, University of Cologne, and of the University of Massachusetts Medical School and kept under a 12 h light cycle, and given a regular chow diet (Harlan diet no. 2918 or Prolab Isopro RMH3000 5P76) *ad libitum*. Germ-free mice were produced at the gnotobiotic facilities of the University of Ulm and of the Hannover Medical School. All animal procedures were conducted in accordance with European, national and institutional guidelines and protocols were approved by local government authorities (Landesamt für Natur, Umwelt und Verbraucherschutz Nordrhein-Westfalen, Germany). Animals requiring medical attention were provided with appropriate care and excluded from the experiments described. No other exclusion criteria existed. For antibiotic treatment of RIPK1$^{IEC\text{-}KO}$ mice one of two different broad spectrum antibiotic mixtures was added to the drinking water starting from embryonic day (E)17.5: 1 g l^{-1} ampicillin (ICN Biomedicals), 1 g l^{-1} neomycin (Sigma), 0.5 g l^{-1} Meronem (AstraZeneca) and 0.5 g l^{-1} ciprofloxacin (Fluka) or 1 g l^{-1} ampicillin (ICN Biomedicals), 1 g l^{-1} metronidazole (Sigma), 0.5 g l^{-1} vancomycin (Eberth) and 0.2 g l^{-1} ciprofloxacin (Fluka). In VillinCreER^{T2}/*Ripk1*$^{fl/fl}$ mice a modified version of the first protocol was employed, where Meronem was replaced by 0.5 g l^{-1} vancomycin (Eberth). As neither the overall physiological response nor tissue pathology differed between the two regimens, mouse groups receiving either antibiotic mixture were analysed together and data from individual experiments were pooled. VillinCreER^{T2} recombinase activity was induced by three daily intraperitoneal administrations of 1 mg tamoxifen. Littermates not carrying the Villin-Cre, Villin-CreER^{T2} and K14-Cre transgenes were used as controls in all experiments. Mice of the indicated genotype were assigned at random to groups. Mouse studies were performed in a blinded fashion. Unless otherwise indicated, mice were analysed at 3 weeks of age. Groups included male and female animals.

Targeting of the *Mlkl* gene in zygotes from RIPK1$^{E\text{-}KO}$ mice

Fertilized oocytes obtained from breedings of *K14-Cre; Ripk1*$^{fl/wt}$ males with *Ripk1*$^{fl/fl}$ females were microinjected with *Mlkl* short guiding (sg)RNA and *Cas9* mRNA. sgRNA and truncated sgRNA were prepared by *in vitro* transcription of T7-promoter and sgRNA targeting sequence containing PCR products. These sgRNA templates were generated using a long sgRNA forward primer containing the T7 promoter (5′-TTAATACGACTCACTATAGG-3′) used for *in vitro* transcription, 20 bp sgRNA(5′-CGTCTAGGAAACCGTGTGCA-3′) or 18 bp sgRNA_TRUNC[39] (5′-TCTAGGAAACCGTGTGCA-3′) targeting sequence and 20 bp homology to the px330 template (5′-GTTTTAGAGCTAGAAATAGC-3′; Zhang laboratory, Addgene plasmid 42230). The forward primer for MLKL_sgRNA is 5′-TTAATACGACTCACTATAGGCGTCTAGGAAACCGTGTGCAGTTTTAGAGCTAGAAATAGC-3′ and the forward primer for MLKL_sgRNA_TRUNC is 5′-TTAATACGACTCACTATAGGTCTAGGAAACCGTGTGCAGTTTTAGAGCTAGAAATAGC-3′. The long forward primers were used together with sgRNA_rev (5′-AAAAAGCACCGACTCGGTGCC-3′) to amplify the chimaeric sgRNA template from px330. The resulting 121 bp or 119 bp PCR product (MLKL_sgRNA or MLKL_sgRNA_TRUNC)was used for *in vitro* transcription using the T7 High Yield *in vitro* transcription kit (NEB) and sgRNA was purified using RNA isolation columns (Macherey Nagel). Fertilized oocytes were injected at 0.5 days post-coitum (dpc) with 100

ng μl^{-1} *Cas9* mRNA (TriLink) together with 50 ng μl^{-1} sgRNA and the surviving two-cell-stage embryos were transferred the next day to foster mothers. Progeny was genotyped using the following primers: typing_fwd, 5′-GTCTTGCACGGTGGAGGTAT-3′; typing_rev, 5′-CCCAGACGTCTCTCAGCTTC-3′, and the T7 endonuclease I assay. Briefly, PCR product was boiled for 10 min at 98 °C and annealed by slowly cooling down to room temperature. The reaction was subsequently incubated with T7 endonuclease I (NEB) and analysed on a 2% agarose gel. Appearance of additional bands indicated mutations at the *Mlkl* locus. Additionally the PCR product was subjected to ApaLI restriction (NEB) with a lack of cleavage indicating the presence of a mutation. Mutations in the *Mlkl* locus were identified by sequencing the PCR product (GATC-Biotech).

IEC isolation and immunoblotting

IECs were isolated by sequential incubation of intestinal tissue in 1 mM dithiothreitol (DTT) and 1.5 mM EDTA solutions as described previously[40]. Cell lysates from IECs and keratinocytes were prepared as described[41,42]. Lysis buffer was supplemented with protease and phosphatase inhibitor tablets (Roche). Cell lysates were separated on SDS–PAGE and transferred to PVDF membranes (IPVH00010, Millipore). Membranes were probed with primary antibodies against the following proteins: RIPK1 (610459, BD Biosciences), RIPK3 (ADI-905-242-100), cIAP1 (ALX-803-335-C100, Enzo), IκBα (sc-371), TRAF2 (sc-876), TRAF3 (sc-949), TRADD (sc-7868), p65 (sc-372), c-Rel (sc-71),HDAC1 (sc-7872), β-actin, (sc-1616, Santacruz), phospho-p65 (3033), JNK (9252), RelB (4922), phospho-p38 (9211), p38 (8690), phospho-ERK (9101), ERK (9102, Cell Signaling), phospho-JNK (44-682G, Invitrogen), p100/52 (NR1495), p105/50 (NR1157, NCI BRB), α-tubulin (T6074, Sigma), TRAF6 (597, MBL), c-FLIP (AG-20B-0005-C100, Adipogen), followed by secondary HRP-coupled antibodies (GE Healthcare and Jackson ImmuneResearch) and developed with chemiluminescent detection substrate (GE Healthcare and Thermo Scientific).

Isolation of lamina propria cells and flow cytometry

Colon and small intestine lamina propria cells were isolated using a modified version of a previously described protocol[43]. In brief, after removal of Peyer's patches, small intestine and colon tissues were incubated at 37 °C in HBSS containing 4% FCS, 10 mM HEPES and 5 mM EDTA. The remaining tissue was cut into small pieces and digested in HBSS containing 4% FCS, 10 mM HEPES, Dispase II (0.15 mg ml^{-1}; Roche), Collagenase D (0.4 mg ml^{-1}; Roche) and DNase I (0.5 mg ml^{-1}; Sigma-Aldrich). The isolated cells were purified by Percoll gradient centrifugation (GE Healthcare Life Sciences). Single-cell suspensions were preincubated with CD16/CD32 antibody (BD Biosciences) for Fc-receptor blocking and subsequently stained with the following fluorescently labelled antibodies: CD3e (145-2C11), CD11b (M1/70), CD45.2 (104), Ly6G (1A8), B220 (RA3-6B2), F4/80 (BM8) (BD Biosciences or eBioscience). Experiments were acquired on a BD FACS Canto I (BD Biosciences) interfaced to FACSDiva software (BD), and analysed with FlowJo software (Tree Star).

Histology

Intestinal tissues were fixed in 4% paraformaldehyde, skin samples in 10% formalin and embedded in paraffin and cut in 3–5 μm sections. Paraffin sections were rehydrated and

heat-induced antigen retrieval was performed in citrate buffer, TRIS buffer or by proteinase K treatment. Primary antibodies for immunohistochemistry were anti-CD45 (550566, eBioscience), anti-Gr-1 (551459, BD Biosciences and MCATTIGA, Serotec), anti-F4/80 (clone A3-1, homemade), anti-B220 (clone RA36B2, homemade), anti-CD3(ab5690, Abcam), anti-active caspase 3 (9661, Cell signalling and AF835, R&D Systems), anti-Ki67 (M724901, Dako), anti-human lysozyme (A0099, Dako). Biotinylated secondary antibodies were purchased from Perkin Elmer and Dako. Stainings were visualized with ABC Kit Vectastain Elite (Vector Laboratories) or Streptavidin-HRP (Millipore) and DAB substrate (DAKO and Vector Laboratories). Incubation times with DAB substrate were equal for all samples. Periodic acid–Schiff (PAS) reaction was performed according to standard protocols. Endogenous alkaline phosphatase activity was visualized using Vector Red Alkaline Phosphatase Substrate Kit according to the manufacturer's instructions (SK-5100, Vector Laboratories). Immunostainings on skin sections were performed as previously described[42], Gr-1 staining was performed on cryo-sections. For assessment of intestinal pathology, H&E-stained intestinal sections were subjected blindly to a semiquantitative composite histological pathology scoring system as described previously[44]. Microscopic quantification of epidermal thickness was performed by measurement of epidermal thickness in four different back skin areas for each mouse. In each field, four measurements were performed. The percentage of the inflamed area was determined by measuring the cumulative number of the inflamed areas in relation to the total area of one section from back skin of each mouse. The number of $CC3^+$ and $CC3^-$ dying cells was determined on the same skin section by staining with anti-CC3 antibodies and counterstaining with H&E. Dying $CC3^-$ keratinocytes were identified by their pyknotic nuclei and eosinophilic cytoplasm.

Near native imaging

Sections for imaging of mCherry at near native conditions were prepared as described[45]. Briefly, the intestine was dissected, thoroughly rinsed and fixed in 4% PFA for 20 min at room temperature. Tissue was embedded in 4% low melting agarose and sectioned with a vibrating blade microtome (Leica) at 150 μm. Permeabilization and staining were performed in PBS supplemented with 1% (wt/vol) BSA, 1% (vol/vol) dimethylsulphoxide (DMSO) and 2% (vol/vol) Triton X-100. Paneth cells were visualized with anti-lysozyme antibody and goat anti-rabbit IgG Alexa-488 (Molecular Probes, A11008). Images of fluorescent stainings were acquired with a Zeiss Meta 510 confocal laser-scanning microscope.

Isolation and culture of primary murine keratinocytes

Isolation and culture of primary murine keratinocytes was performed as described previously[46].

Isolation and culture of intestinal organoids

Small intestinal crypts were isolated and grown to organoids as described previously[47]. Deletion of RIPK1 in organoid cultures from $RIPK1^{tamIEC\text{-}KO}$ mice was induced by addition of 100 nM 4-OH-tamoxifen (4-OHT) to the culture medium for 20–24 h. Cell death of organoid cultures was determined by quantification of propidium iodine (PI)-positive cells by flow cytometry acquired on a FACSCalibur, BD. For qRT–PCR analysis organoids were

harvested 36 h after 4-OHT removal. For each genotype, organoids from two different mice were enrolled, seeded out in quadruplicates and processed independently.

qRT–PCR

Total RNA was extracted with Trizol Reagent (Life Technologies) and RNeasy Columns (Qiagen) and cDNA was prepared with Superscript III cDNA-synthesis Kit (Life Technologies). qRT–PCR was performed with TaqMan probes (Life Technologies) with TATA-box-binding protein as reference gene for intestinal samples and HRPT for skin tissue. Data were analysed according to the ΔCT method. Primer sequences are available upon request.

Statistics

Data shown in column graphs represent the mean ± s.d. or ± s.e.m., as indicated in the figure legends. To determine the group size necessary for adequate statistical power, power analysis was performed using preliminary data sets. When data fulfilled the criteria for Gaussian distribution, unpaired Student's *t*-tests were performed; otherwise the nonparametric Mann–Whitney test was chosen. For the keratinocyte viability assay, a paired Student's *t*-test was performed. $*P \leq 0.05$, $**P \leq 0.01$, $***P \leq 0.005$. Statistical analysis was performed with Prism6, GraphPad or Excel, Microscoft software.

Extended Data

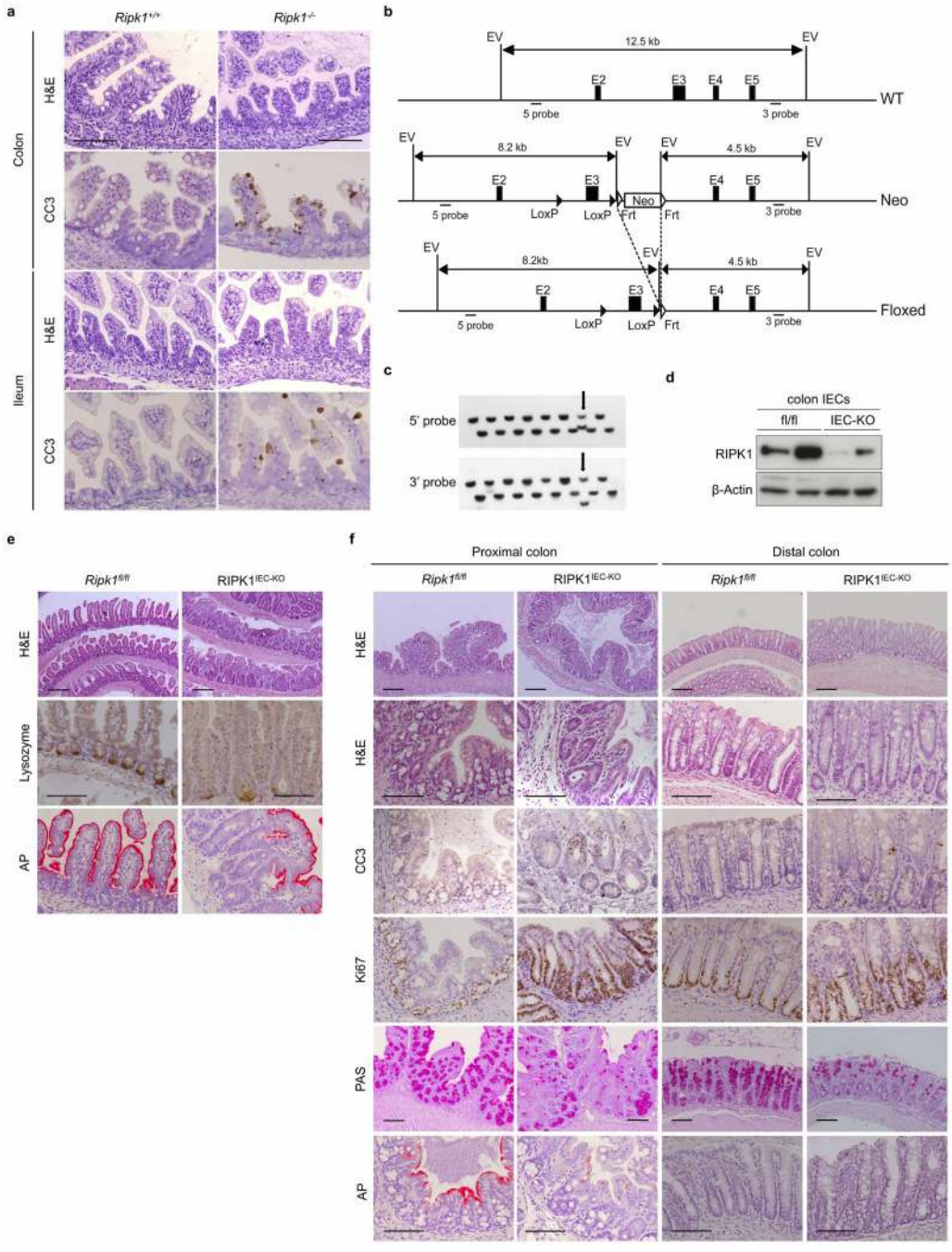

Extended Data Figure 1. Intestinal pathology in Ripk1$^{-/-}$ and RIPK1$^{IEC\text{-}KO}$ mice

a, Representative images of colonic and ileal sections from newborn *Ripk1*$^{+/+}$ and *Ripk1*$^{-/-}$ mice stained with H&E or immunostained for CC3. **b**, Targeting strategy for the generation of mice with *loxP*-flanked (floxed (fl)) *Ripk1* alleles. Exon 3 of the *Ripk1* gene was flanked with *loxP* sites and an FRT-flanked neomycin (Neo) selectable cassette was introduced after the 3′ *loxP* site. The Neo cassette was excised by crossing the *Ripk1*^{neoFloxed} mice with Flp-

deleter mice. **c**, Representative Southern blots depicting the identification of correctly targeted embryonic stem (ES) cell clones by using 5′ and 3′ external probes. Arrows indicate a correctly targeted ES cell clone. Screening for the *loxP* site in intron 2 was performed by PCR (data not shown). Double combs allowing loading samples at two levels were used to maximize loading capacity of the gels for screening ES clones in 96-well plates. **d**, Immunoblot of colon IEC protein extracts from $Ripk1^{fl/fl}$ and $RIPK1^{IEC\text{-}KO}$ mice. **e**, **f**, Representative images of ileal (**e**) or colon (**f**) sections from $Ripk1^{fl/fl}$ and $RIPK1^{IEC\text{-}KO}$ mice stained with H&E, PAS or alkaline phosphatase (AP), or immunostained against lysozyme, CC3 or Ki67. Scale bars, 100 μm.

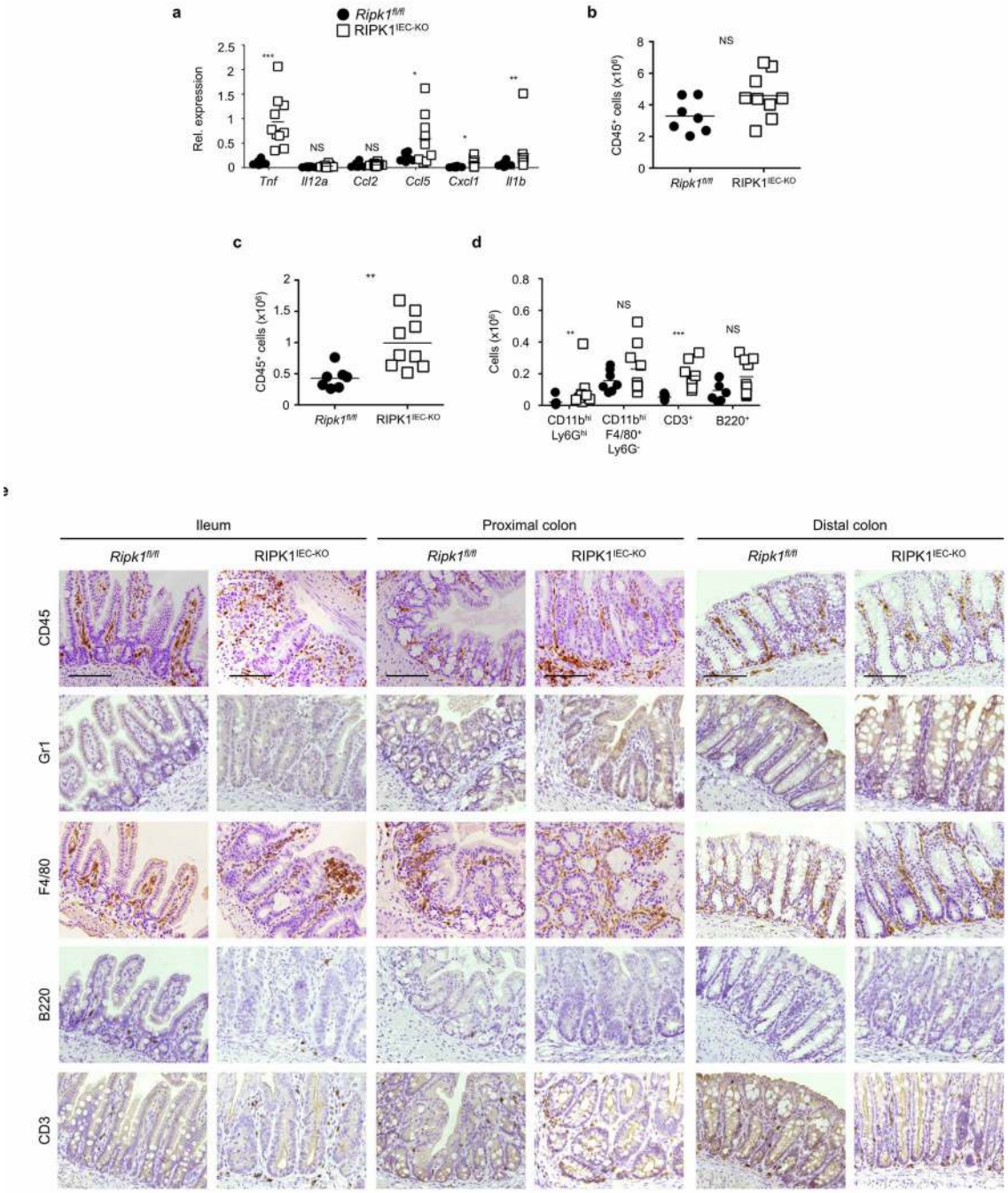

Extended Data Figure 2. Mild intestinal inflammation in RIPK1^{IEC-KO} mice

a, qRT–PCR analysis of cytokine and chemokine expression in colon tissue from *Ripk1*$^{fl/fl}$ and RIPK1^{IEC-KO} mice. **b–d**, FACS analysis of lamina propria leukocytes in the small intestine (**b**) and colon (**c**, **d**) of *Ripk1*$^{fl/fl}$ and RIPK1^{IEC-KO} mice. **e**, Representative images from intestinal sections from *Ripk1*$^{fl/fl}$ and RIPK1^{IEC-KO} mice immunostained with the indicated antibodies. Scale bars, 100 μm. *P ≤0.05, **P ≤0.01, ***P ≤0.005; NS, not significant.

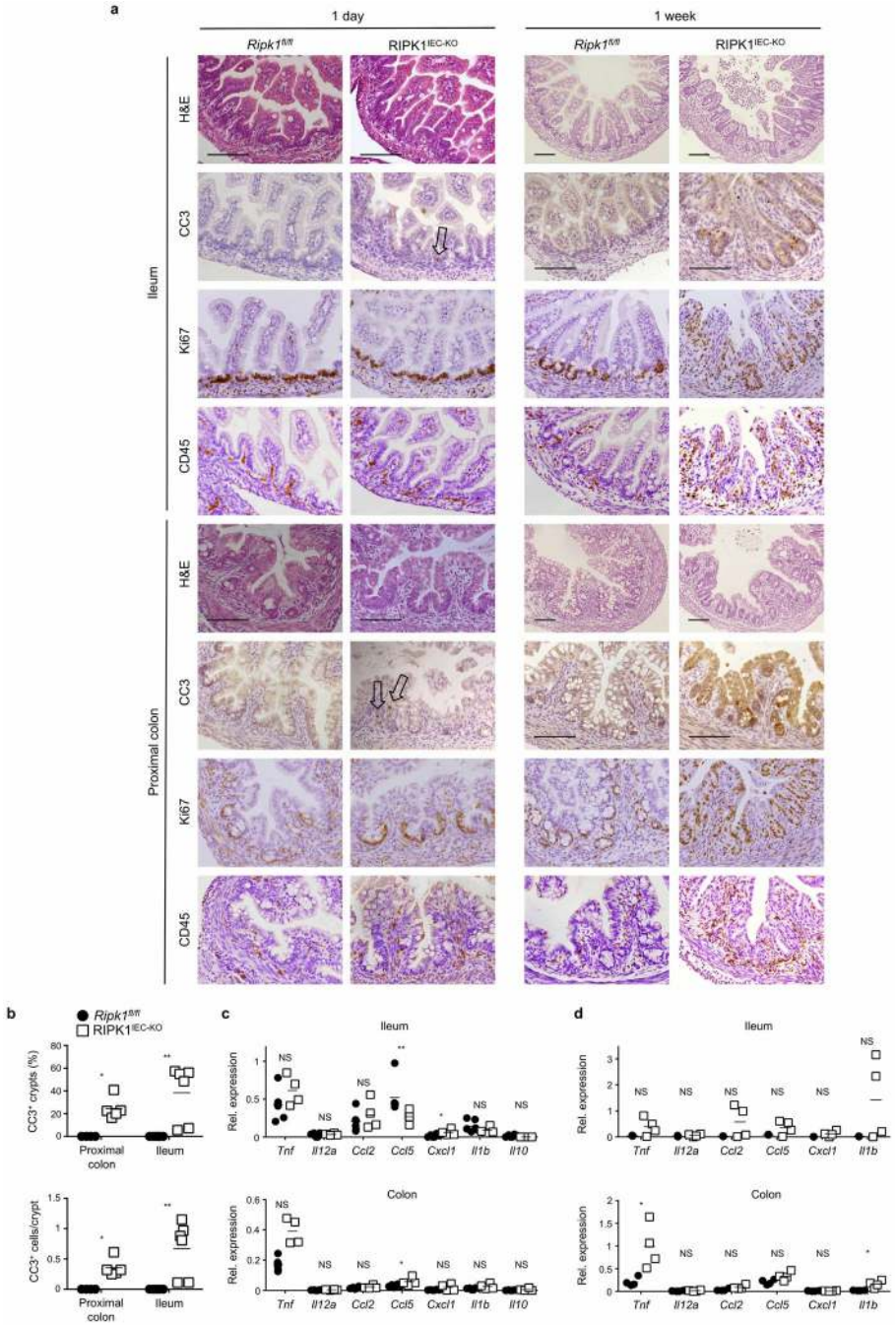

Extended Data Figure 3. Assessment of intestinal pathology in newborn and 1-week-old RIPK1^{IEC-KO} mice

a, Representative images of intestinal sections from *Ripk1$^{fl/fl}$* and RIPK1^{IEC-KO} mice stained with H&E or immunostained with the indicated antibodies. Arrows indicate sparse CC3^{+} IECs in sections from 1-day-old animals. Scale bars, 100 μm. **b**, Quantification of crypts containing CC3^{+} cells and the number of CC3^{+} cells per crypt in intestinal sections of 1-week-old *Ripk1$^{fl/fl}$* and RIPK1^{IEC-KO} mice. **c**, **d**, qRT–PCR analysis of cytokine and chemokine expression in small intestinal and colon tissue from 1-day-old (**c**) and 1-week-old

(**d**) *Ripk1*$^{fl/fl}$ and RIPK1$^{IEC\text{-}KO}$ mice. *P ≤0.05, **P ≤0.01, ***P ≤0.005; NS, not significant.

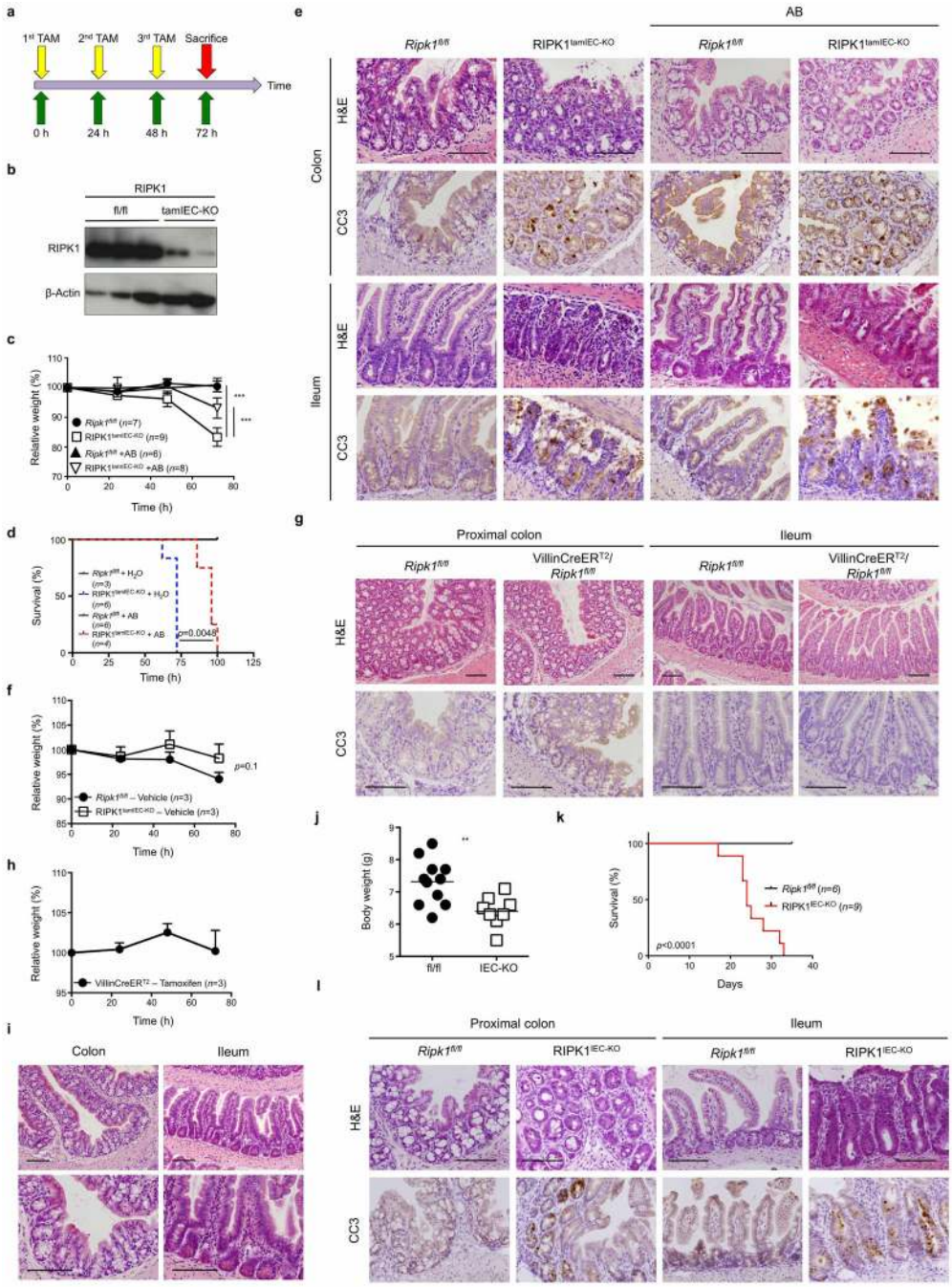

Extended Data Figure 4. Antibiotic treatment does not prevent intestinal pathology in RIPK1$^{IEC\text{-}KO}$ and RIPK1$^{tamIEC\text{-}KO}$ mice

a, Experimental outline of tamoxifen injections (TAM; 1 mg, intraperitoneally). **b**, Immunoblot of small intestine IEC protein extracts from tamoxifen-treated *Ripk1*$^{fl/fl}$ and RIPK1$^{tamIEC\text{-}KO}$ mice. **c**–**e**, Body weight change (**c**), Kaplan–Meier survival curve (**d**) and representative images of H&E- and CC3-stained intestinal sections (**e**) of tamoxifen-treated

Ripk1$^{fl/fl}$ and RIPK1$^{tamIEC\text{-}KO}$ mice receiving antibiotics (+AB) or normal drinking water starting 4 weeks before tamoxifen administration. **f**, **g**, Body weight change (**f**) and representative images of H&E- and CC3-stained intestinal sections (**g**) in vehicle-injected *Ripk1*$^{fl/fl}$ and RIPK1$^{tamIEC\text{-}KO}$ mice. **h**, **i**, Body weight changes (**h**) and representative images of H&E-stained intestinal sections (**i**) of tamoxifen-injected Villin-CreER^{T2} mice (n = 3). **j**–**l**, Body weight (**j**), Kaplan–Meier survival curve (**k**) and representative images of H&E- and CC3-stained intestinal sections (**l**) of *Ripk1*$^{fl/fl}$ and RIPK1$^{IEC\text{-}KO}$ mice treated with antibiotics from E17.5 to 3 weeks of age. Scale bars, 100 μm. Error bars represent mean values ± s.d. *P ≤0.05, **P ≤0.01, ***P ≤0.005; NS, not significant.

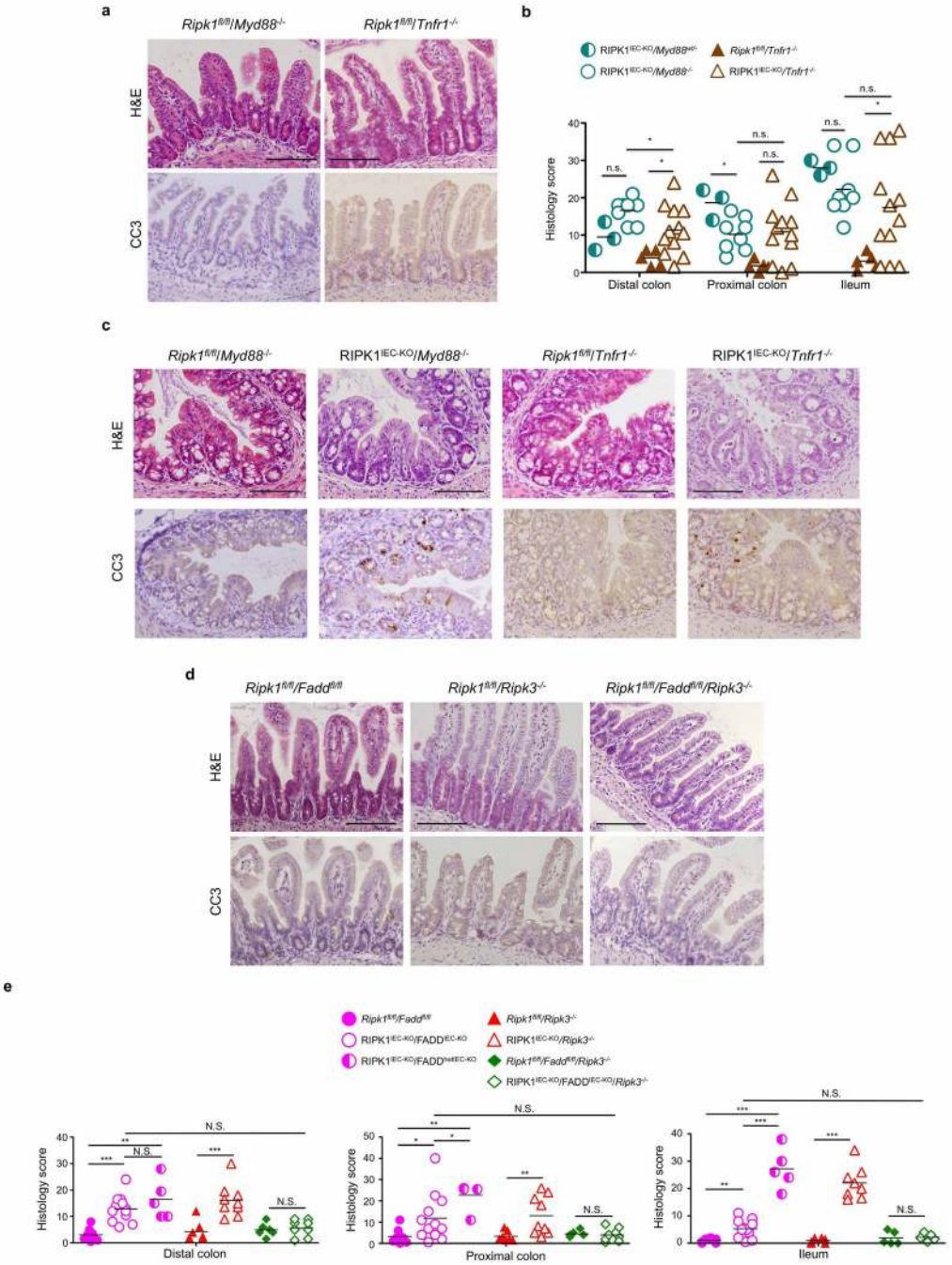

Extended Data Figure 5. Role of MyD88, TNFR1, FADD and RIPK3 in the intestinal pathology of RIPK1$^{IEC\text{-}KO}$ mice

a, Representative images of ileal sections from the indicated mice as controls for the mice shown in Fig. 2a. **b**, Quantification of histological pathology score of the indicated mice. **c**, Representative images of H&E- or CC3-stained colon sections from the indicated mice. **d**, Representative images of H&E- or CC3-stained ileal sections from the indicated mice. Scale bars, 100 μm. **e**, Quantification of histological pathology score of the indicated mice. *$P \leq 0.05$, **$P \leq 0.01$, ***$P \leq 0.005$; NS, not significant.

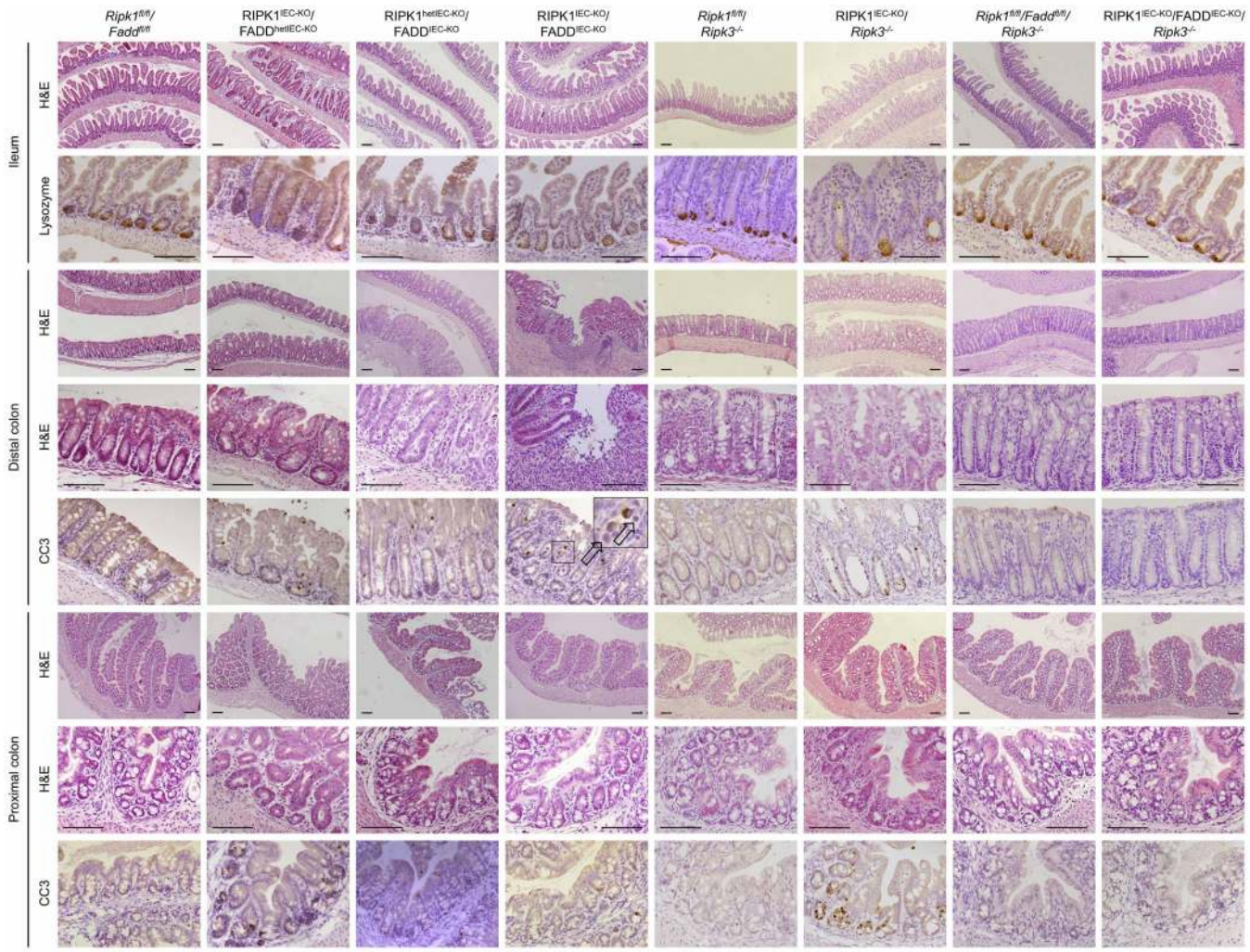

Extended Data Figure 6. Epithelial-specific FADD deficiency reduces IEC apoptosis, ameliorates crypt atrophy but triggers erosive lesions in the colon of RIPK1^{IEC-KO} mice

Representative images of ileal and colonic sections from the indicated mice stained with H&E or immunostained against lysozyme or CC3. Scale bars, 100 μm.

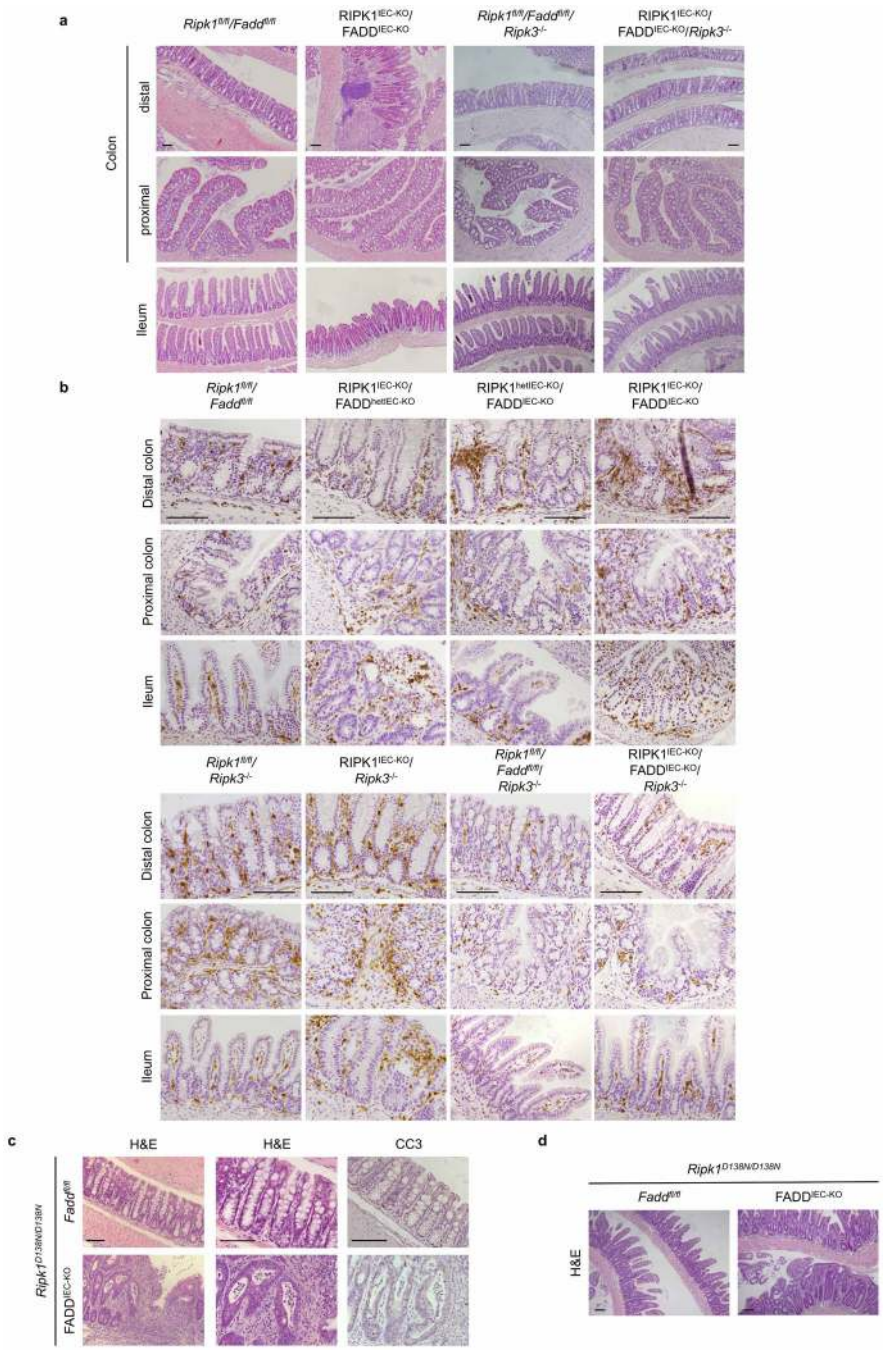

Extended Data Figure 7. FADD and RIPK3 deficiency restores intestinal homeostasis in RIPK1^{IEC-KO} mice and IEC necroptosis in FADD^{IEC-KO} mice occurs in the absence of RIPK1 kinase activity

a, Representative images of H&E-stained colonic and ileal sections of adult mice with the indicated genotypes. **b**, Representative images of colonic and ileal sections of mice with the indicated genotypes immunostained for CD45. **c**, **d**, Representative images of colonic (**c**) and ileal (**d**) sections of adult *Fadd$^{fl/fl}$/Ripk1$^{D138N/D138N}$* and FADD^{IEC-KO}/ *Ripk1$^{D138N/D138N}$* mice stained with H&E or immunostained against CC3. Scale bars, 100 μm.

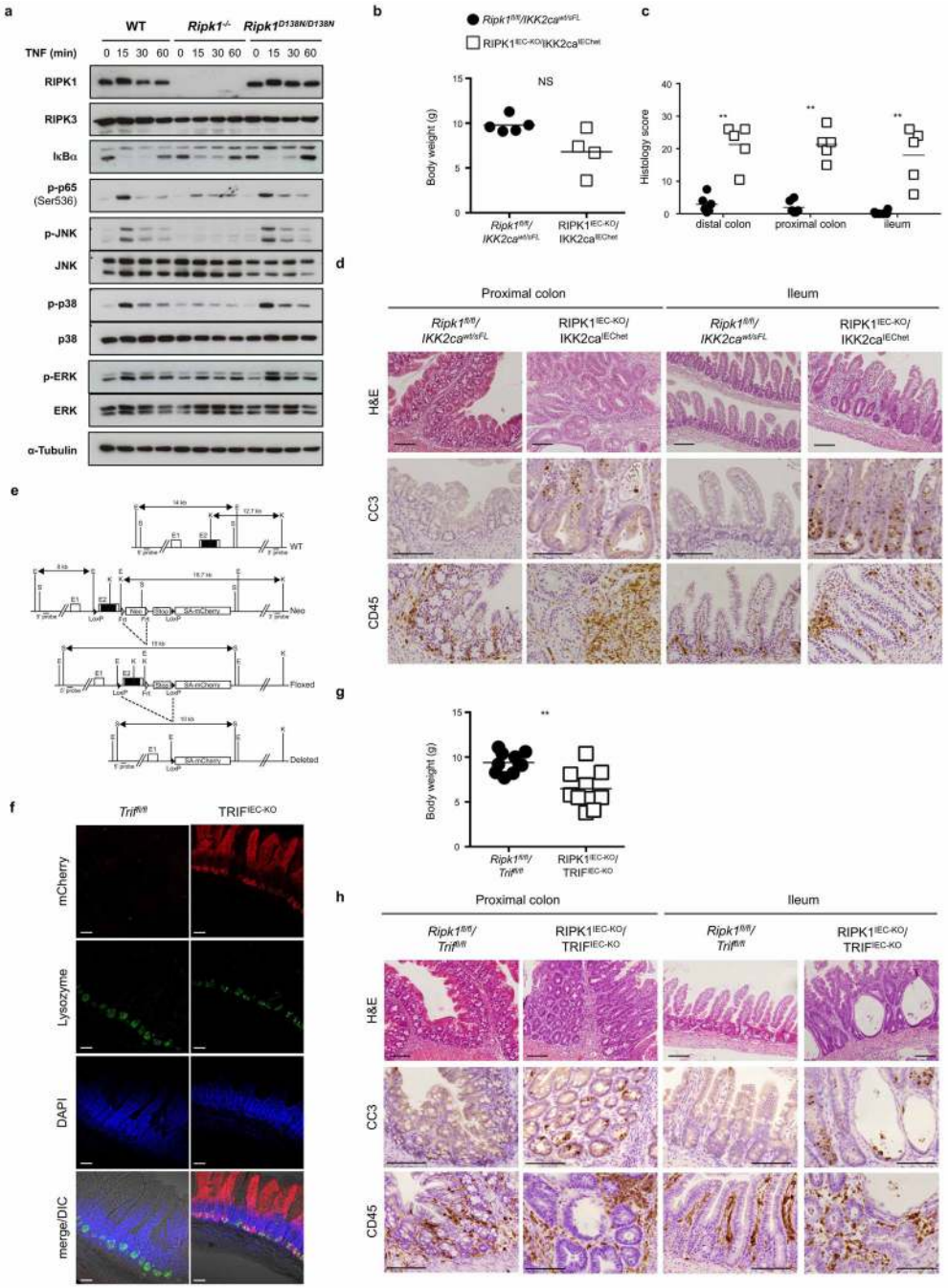

Extended Data Figure 8. Assessment of the role of NF-κB and TRIF signalling in RIPK1^{IEC-KO} mice

a, Immunoblot analysis of protein extracts from wild-type (WT), *Ripk1*$^{-/-}$ and *Ripk1*$^{D138N/D138N}$ MEFs after stimulation with 10 ng ml^{-1} recombinant murine TNF for the indicated time points. Data are representative of five independent experiments. **b**–**d**, Body weight (**b**), quantification of histological pathology score (**c**) and representative H&E-, CC3- or CD45-stained intestinal sections (**d**) of mice with the indicated genotypes. **e**, Targeting strategy used for the generation of *Trif*$^{fl/fl}$ mice. Exon 2 of the *Trif* gene was flanked with

loxP sites. FRT-flanked neo and a stop cassette were placed upstream of the 3′ *loxP* site. A splice acceptor (SA)-mCherry cassette was introduced downstream of the 3′ *loxP* site. Cre-mediated recombination removes the *Trif* coding sequences and the stop cassette inducing the expression of mCherry by the *Trif* locus. The FRT-flanked neo was excised by crossing $Trif^{\text{neoFloxed}}$ mice with Flp-Deleter mice. **f**, Confocal microscopy images of near native small intestinal sections of $Trif^{fl/fl}$ and $\text{TRIF}^{\text{IEC-KO}}$ mice stained with anti-lysozyme and DAPI. **g**, **h**, Body weight (**g**) and representative images of H&E-, CC3- or CD45-stained intestinal sections (**h**) of the indicated mice. Scale bars, 100 μm. $^{*}P \leq 0.05$, $^{**}P \leq 0.01$, $^{***}P \leq 0.005$; NS, not significant.

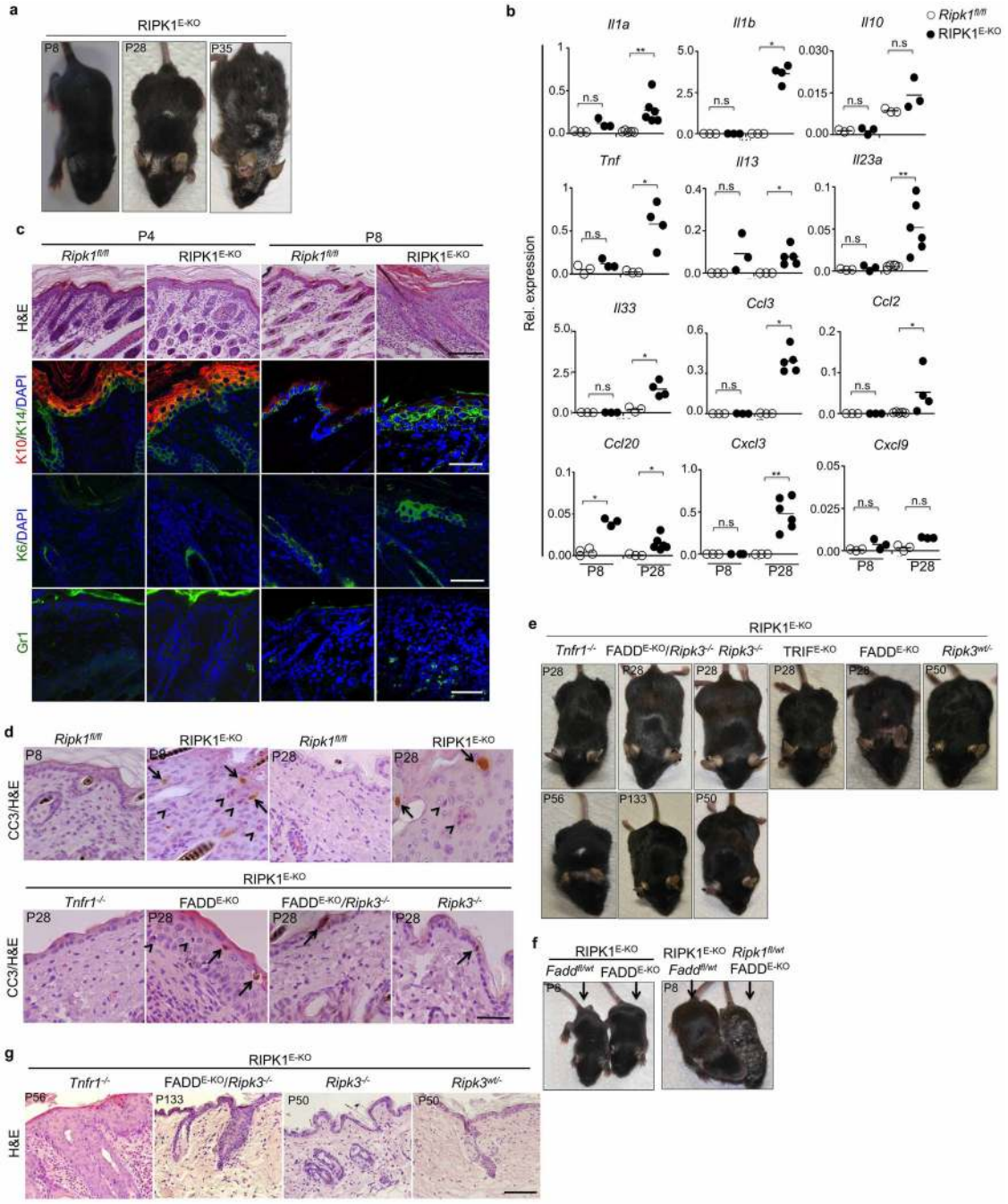

Extended Data Figure 9. Skin inflammation in RIPK1$^{E\text{-}KO}$ mice is dependent on RIPK3-mediated necroptosis

a, Representative macroscopic images of RIPK1$^{E\text{-}KO}$ mice. **b**, qRT–PCR analysis of pro-inflammatory cytokines and chemokines on total skin mRNA from *Ripk1$^{fl/fl}$* and RIPK1$^{E\text{-}KO}$ mice. **c**, **d**, Representative images of skin sections from the indicated mice stained as indicated. In **d**, arrows point to CC3^{+} cells and arrowheads depict CC3^{-} dying cells identified by their pyknotic nuclei and eosinophilic cytoplasm. Scale bars, 100 μm in H&E stained; 50 μm in immunostained sections. **e**–**g**, Representative macroscopic pictures

(**e**, **f**) and H&E-stained skin sections (**g**) of the indicated mice. Scale bars, 100 μm. *$P \leq$ 0.05, **$P \leq$0.01, ***$P \leq$0.005; NS, not significant.

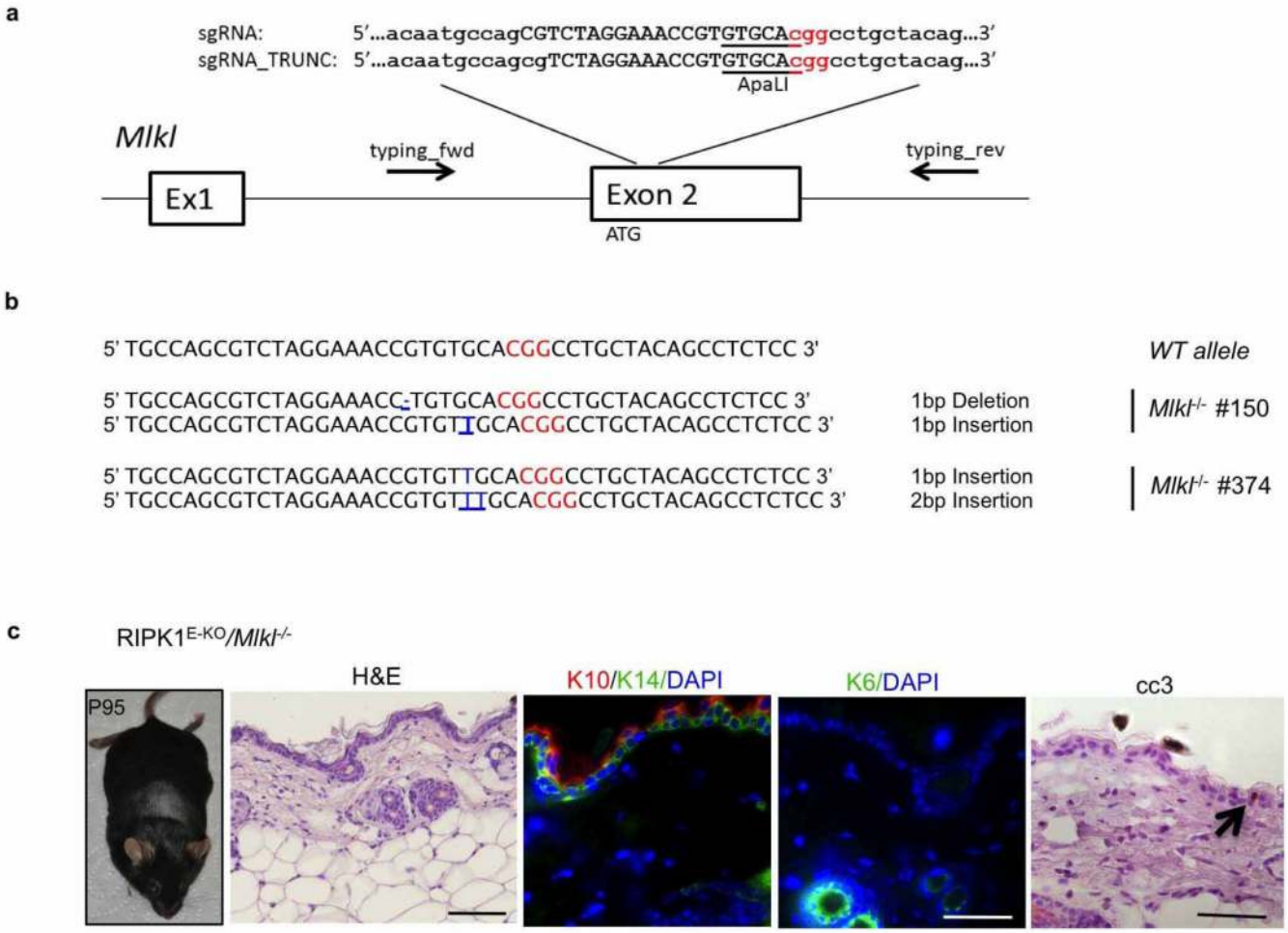

Extended Data Figure 10. CRISPR/Cas9-mediated knockout of MLKL prevents skin inflammation in RIPK1$^{E\text{-}KO}$ mice

a, Schematic depiction of the *Mlkl* locus. The sequence targeted by the small guide RNAs (sgRNA and truncated TRUNC_sgRNA) is indicated by capital letters. The position of the ATG and the binding sites of the primers used for genotyping and sequencing are indicated. The sgRNAs were designed to target a sequence containing an ApaLI restriction site that is used for RFLP analysis (underlined). The protospacer-adjacent motif (PAM) sequence is depicted in red. **b**, Sequences of the wild-type (WT) *Mlkl* locus and of the targeted *Mlkl* alleles of the two obtained RIPK1$^{E\text{-}KO}$/*Mlkl*$^{-/-}$ mice. Mouse #150 carries one allele with one base pair (bp) deletion and one allele with one bp insertion. Mouse #374 carries one allele with one bp insertion and one allele with two bp insertions. All mutations cause frame shift and ablate MLKL protein expression. Mouse #150 was obtained using the full-length MLKL-sgRNA and mouse #374 was obtained using the truncated MLKL_sgRNA_TRUNC. **c**, Macroscopic appearance and histological images of skin sections from RIPK1$^{E\text{-}KO}$/Mlkl$^{-/-}$ mouse #150 at the age of P95. Scale bars, 100 μm (H&E); 50μm (keratins and CC3).

Acknowledgments

We are grateful to V. Dixit for *Ripk3*$^{-/-}$, D. Gumucio for Villin-Cre and S. Robine for Villin-CreER^{T2} mice. We thank C. Uthoff-Hachenberg, J. Buchholz, E. Mahlberg, B. Kühnel, B. Hülser, P. Jankowski, S. Assenmacher and P. Scholl for technical assistance. M.P. acknowledges funding from the European Research Council (2012-ADG_20120314), the German Research Council (DFG; SFB670, SFB829, SPP1656), the European Commission (grants 223404 (Masterswitch) and 223151 (InflaCare)), the Deutsche Krebshilfe, the Else Krüner-Fresenius-Stiftung and the Helmholtz Alliance (PCCC). Research reported in this publication was also supported by the National Institute of Allergy and Infectious Diseases division of the National Institutes of Health under award RO1AI075118 to M.K.

References

1. Oberst A, et al. Catalytic activity of the caspase-8–FLIP$_L$ complex inhibits RIPK3-dependent necrosis. Nature. 2011; 471:363–367. [PubMed: 21368763]
2. Kaiser WJ, et al. RIP3 mediates the embryonic lethality of caspase-8-deficient mice. Nature. 2011; 471:368–372. [PubMed: 21368762]
3. Zhang H, et al. Functional complementation between FADD and RIP1 in embryos and lymphocytes. Nature. 2011; 471:373–376. [PubMed: 21368761]
4. Bonnet MC, et al. The adaptor protein FADD protects epidermal keratinocytes from necroptosis *in vivo* and prevents skin inflammation. Immunity. 2011; 35:572–582. [PubMed: 22000287]
5. Welz PS, et al. FADD prevents RIP3-mediated epithelial cell necrosis and chronic intestinal inflammation. Nature. 2011; 477:330–334. [PubMed: 21804564]
6. Dillon CP, et al. Survival function of the FADD-CASPASE-8-cFLIP(L) complex. Cell Rep. 2012; 1:401–407. [PubMed: 22675671]
7. Duprez L, et al. RIP kinase-dependent necrosis drives lethal systemic inflammatory response syndrome. Immunity. 2011; 35:908–918. [PubMed: 22195746]
8. Upton JW, Kaiser WJ, Mocarski ES. Virus inhibition of RIP3-dependent necrosis. Cell Host Microbe. 2010; 7:302–313. [PubMed: 20413098]
9. Kelliher MA, et al. The death domain kinase RIP mediates the TNF-induced NF-κB signal. Immunity. 1998; 8:297–303. [PubMed: 9529147]
10. Cusson-Hermance N, Khurana S, Lee TH, Fitzgerald KA, Kelliher MA. Rip1 mediates the Trif-dependent toll-like receptor 3- and 4-induced NF-κB activation but does not contribute to interferon regulatory factor 3 activation. J. Biol. Chem. 2005; 280:36560–36566. [PubMed: 16115877]
11. Meylan E, et al. RIP1 is an essential mediator of Toll-like receptor 3-inducedNF-κB activation. Nature Immunol. 2004; 5:503–507. [PubMed: 15064760]
12. Kawai T, et al. IPS-1, an adaptor triggering RIG-I- and Mda5-mediated type I interferon induction. Nature Immunol. 2005; 6:981–988. [PubMed: 16127453]
13. Rajput A, et al. RIG-I RNA helicase activation of IRF3 transcription factor is negatively regulated by caspase-8-mediated cleavage of the RIP1 protein. Immunity. 2011; 34:340–351. [PubMed: 21419663]
14. Christofferson DE, Li Y, Yuan J. Control of life-or-death decisions by RIP1 kinase. Annu. Rev. Physiol. 2014; 76:129–150. [PubMed: 24079414]
15. Vanden Berghe T, Linkermann A, Jouan-Lanhouet S, Walczak H, Vandenabeele P. Regulated necrosis: the expanding network of non-apoptotic cell death pathways. Nature Rev. Mol. Cell Biol. 2014; 15:135–147. [PubMed: 24452471]
16. Hill DA, Artis D. Intestinal bacteria and the regulation of immune cell homeostasis. Annu. Rev. Immunol. 2010; 28:623–667. [PubMed: 20192812]
17. Kaser A, Zeissig S, Blumberg RS. Inflammatory bowel disease. Annu. Rev. Immunol. 2010; 28:573–621. [PubMed: 20192811]
18. Lee TH, Shank J, Cusson N, Kelliher MA. The kinase activity of Rip1 is not required for tumor necrosis factor-α-induced IκB kinase or p38 MAP kinase activation or for the ubiquitination of Rip1 by Traf2. J. Biol. Chem. 2004; 279:33185–33191. [PubMed: 15175328]

19. Greten FR, et al. IKKβ links inflammation and tumorigenesis in a mouse model of colitis-associated cancer. Cell. 2004; 118:285–296. [PubMed: 15294155]
20. Nenci A, et al. Epithelial NEMO links innate immunity to chronic intestinal inflammation. Nature. 2007; 446:557–561. [PubMed: 17361131]
21. Steinbrecher KA, Harmel-Laws E, Sitcheran R, Baldwin AS. Loss of epithelial RelA results in deregulated intestinal proliferative/apoptotic homeostasis and susceptibility to inflammation. J. Immunol. 2008; 180:2588–2599. [PubMed: 18250470]
22. Sasaki Y, et al. Canonical NF-κB activity, dispensable for B cell development, replaces BAFF-receptor signals and promotes B cell proliferation upon activation. Immunity. 2006; 24:729–739. [PubMed: 16782029]
23. Vlantis K, et al. Constitutive IKK2 activation in intestinal epithelial cells induces intestinal tumors in mice. J. Clin. Invest. 2011; 121:2781–2793. [PubMed: 21701067]
24. Gentle IE, et al. In TNF-stimulated cells, RIPK1 promotes cell survival by stabilizing TRAF2 and cIAP1, which limits induction of non-canonical NF-κB and activation of caspase-8. J. Biol. Chem. 2011; 286:13282–13291. [PubMed: 21339290]
25. Kim JY, et al. TNFα induced noncanonical NF-κB activation is attenuated by RIP1 through stabilization of TRAF2. J. Cell Sci. 2011; 124:647–656. [PubMed: 21266470]
26. Piao JH, et al. Tumor necrosis factor receptor-associated factor (TRAF) 2 controls homeostasis of the colon to prevent spontaneous development of murine inflammatory bowel disease. J. Biol. Chem. 2011; 286:17879–17888. [PubMed: 21393251]
27. Varfolomeev E, et al. IAP antagonists induce autoubiquitination of c-IAPs, NF-κB activation, and TNFα-dependent apoptosis. Cell. 2007; 131:669–681. [PubMed: 18022362]
28. Vince JE, et al. IAP antagonists target cIAP1 to induce TNFα-dependent apoptosis. Cell. 2007; 131:682–693. [PubMed: 18022363]
29. Polykratis A, et al. Cutting edge: RIPK1 kinase inactive mice are viable and protected from TNF-induced necroptosis *in vivo*. J. Immunol. 2014 http://dx.doi.org/10.4049/jimmunol.1400590.
30. Mc Guire C, et al. Oligodendrocyte-specific FADD deletion protects mice from autoimmune-mediated demyelination. J. Immunol. 2010; 185:7646–7653. [PubMed: 21068410]
31. Rodríguez CI, et al. High-efficiency deleter mice show that FLPe is an alternative to Cre-*loxP*. Nature Genet. 2000; 25:139–140. [PubMed: 10835623]
32. Schwenk F, Baron U, Rajewsky K. A *cre*-transgenic mouse strain for the ubiquitous deletion of *loxP*-flanked gene segments including deletion in germ cells. Nucleic Acids Res. 1995; 23:5080–5081. [PubMed: 8559668]
33. Madison BB, et al. *Cis* elements of the villin gene control expression in restricted domains of the vertical (crypt) and horizontal (duodenum, cecum) axes of the intestine. J. Biol. Chem. 2002; 277:33275–33283. [PubMed: 12065599]
34. El Marjou F, et al. Tissue-specific and inducible Cre-mediated recombination in the gut epithelium. Genesis. 2004; 39:186–193. [PubMed: 15282745]
35. Hafner M, et al. Keratin 14 Cre transgenic mice authenticate keratin 14 as an oocyte-expressed protein. Genesis. 2004; 38:176–181. [PubMed: 15083518]
36. Pfeffer K, et al. Mice deficient for the 55 kd tumor necrosis factor receptor are resistant to endotoxic shock, yet succumb to *L. monocytogenes* infection. Cell. 1993; 73:457–467. [PubMed: 8387893]
37. Adachi O, et al. Targeted disruption of the *MyD88* gene results in loss of IL-1- and IL-18-mediated function. Immunity. 1998; 9:143–150. [PubMed: 9697844]
38. Newton K, Sun X, Dixit VM. Kinase RIP3 is dispensable for normal NF-κBs, signaling by the B-cell and T-cell receptors, tumor necrosis factor receptor 1, and Toll-like receptors 2 and 4. Mol. Cell. Biol. 2004; 24:1464–1469. [PubMed: 14749364]
39. Fu Y, Sander JD, Reyon D, Cascio VM, Joung JK. Improving CRISPR-Cas nuclease specificity using truncated guide RNAs. Nature Biotechnol. 2014; 32:279–284. [PubMed: 24463574]
40. Ukena SN, et al. Probiotic *Escherichia coli* Nissle 1917 inhibits leaky gut by enhancing mucosal integrity. PLoS ONE. 2007; 2:e1308. [PubMed: 18074031]

41. Schmidt-Supprian M, et al. NEMO/IKKγ-deficient mice model incontinentia pigmenti. Mol. Cell. 2000; 5:981–992. [PubMed: 10911992]
42. Kumari S, et al. Tumor necrosis factor receptor signaling in keratinocytes triggers interleukin-24-dependent psoriasis-like skin inflammation in mice. Immunity. 2013; 39:899–911. [PubMed: 24211183]
43. Klose CS, et al. A T-bet gradient controls the fate and function of CCR6^{-}RORγt^{+} innate lymphoid cells. Nature. 2013; 494:261–265. [PubMed: 23334414]
44. Adolph TE, et al. Paneth cells as a site of origin for intestinal inflammation. Nature. 2013; 503:272–276. [PubMed: 24089213]
45. Snippert HJ, Schepers AG, Delconte G, Siersema PD, Clevers H. Slide preparation for single-cell-resolution imaging of fluorescent proteins in their three-dimensional near-native environment. Nature Protocols. 2011; 6:1221–1228.
46. Tscharntke M, et al. Impaired epidermal wound healing *in vivo* upon inhibition or deletion of Rac1. J. Cell Sci. 2007; 120:1480–1490. [PubMed: 17389689]
47. Sato T, et al. Single Lgr5 stem cells build crypt–villus structures *in vitro* without a mesenchymal niche. Nature. 2009; 459:262–265. [PubMed: 19329995]

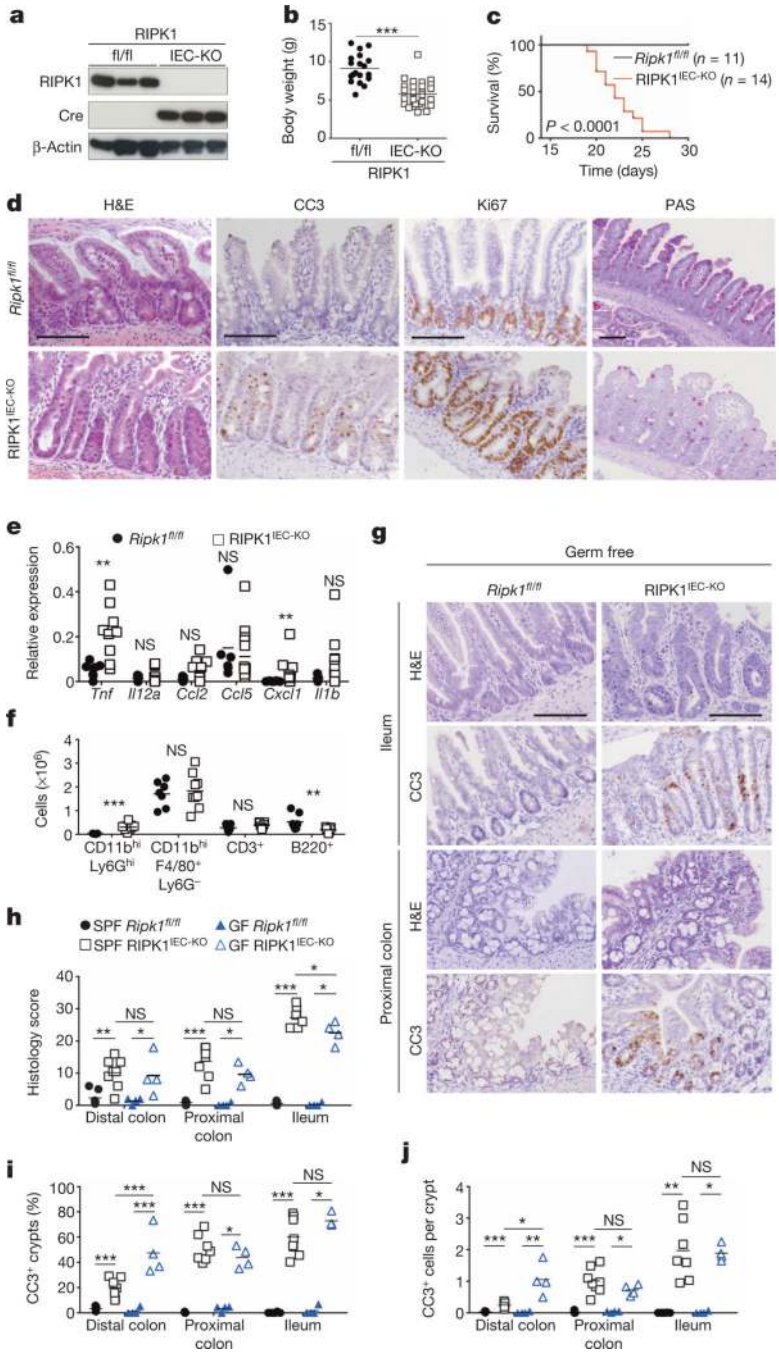

Figure 1. Epithelial RIPK1 ablation causes microbiota-independent intestinal pathology

a, Immunoblot of small intestine IECs from *Ripk1*$^{fl/fl}$ (fl/fl) and RIPK1$^{IEC\text{-}KO}$ (IEC-KO) mice. **b**, **c**, Body weight (**b**) and Kaplan–Meier survival curve (**c**) of *Ripk1*$^{fl/fl}$ and RIPK1$^{IEC\text{-}KO}$ mice. **d**, Representative images of ileal sections from *Ripk1*$^{fl/fl}$ and RIPK1$^{IEC\text{-}KO}$ mice stained as indicated. H&E, haematoxylin and eosin. **e**, **f**, Quantitative polymerase chain reaction with reverse transcription (qRT–PCR) of cytokine and chemokine expression (**e**) and fluorescence-activated cell sorting (FACS) of lamina propria leukocytes (**f**) in the small intestine of *Ripk1*$^{fl/fl}$ and RIPK1$^{IEC\text{-}KO}$ mice. **g**, Representative images of

H&E- or CC3-stained intestinal sections from germ-free *Ripk1*$^{fl/fl}$ and RIPK1$^{IEC\text{-}KO}$ mice. **h**–**j**, Quantification of histological pathology score (**h**), crypts containing CC3^{+} cells (**i**) and CC3^{+} cells per crypt (**j**) in intestinal sections of the indicated mice. GF, germ free; SPF, specific pathogen free. Scale bars, 100 μm. **P* ≤0.05, ***P* ≤0.01, ****P* ≤0.005; NS, not significant.

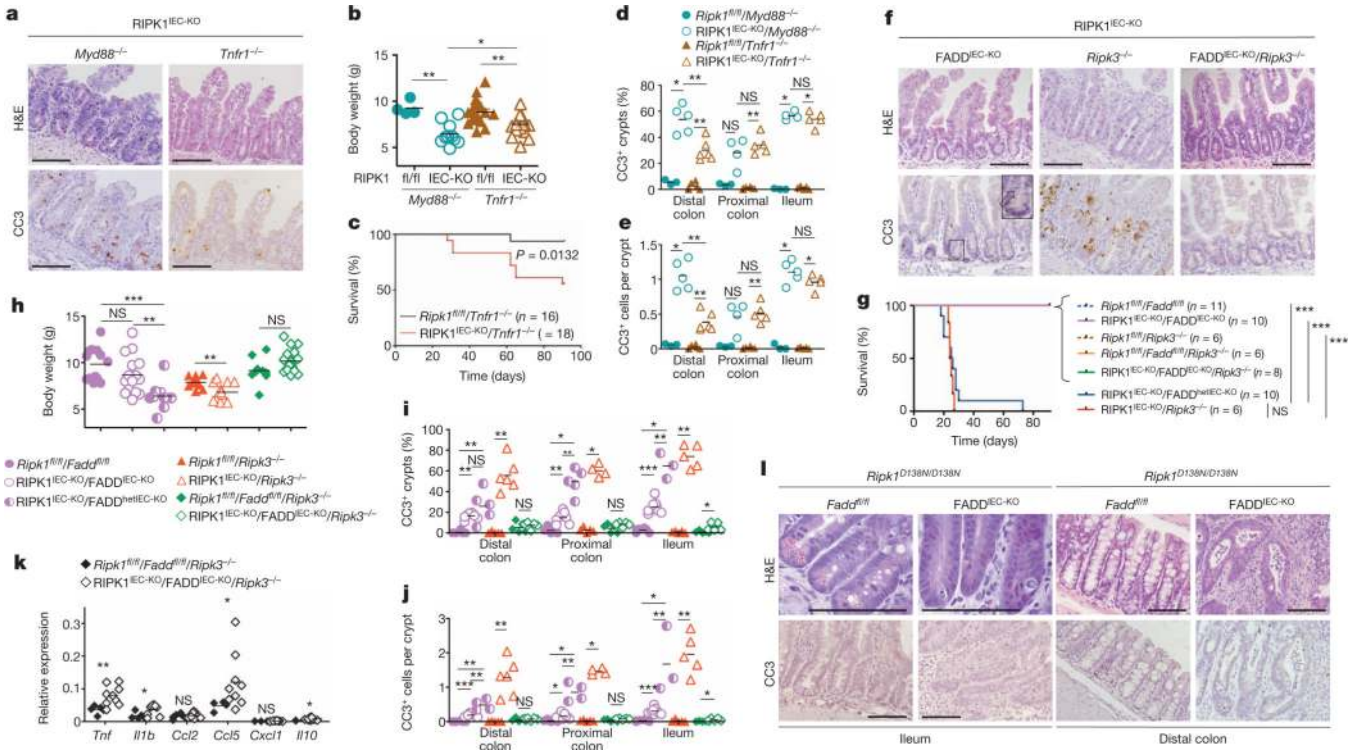

Figure 2. Death of RIPK1-deficient IECs depends on FADD and RIPK3

a, Representative images of H&E- or CC3-stained ileal sections from the indicated mice. **b**, **c**, Body weight (**b**) and Kaplan–Meier survival curve (**c**) of the indicated mice. **d**, **e**, Quantification of crypts containing CC3$^+$ cells (**d**) and CC3$^+$ cell numbers per crypt (**e**) in intestinal sections of the indicated mice. **f**, Representative images of ileal sections from the indicated mice. Arrow depicts CC3$^-$ dying IEC. **g**, **h**, Kaplan–Meier survival curve (**g**) and body weight (**h**) of mice with the indicated genotypes. **i**, **j**, Quantification of crypts containing CC3$^+$ cells (**i**) and CC3$^+$ cell numbers per crypt (**j**) in intestinal sections of the indicated mice. **k**, qRT–PCR analysis of cytokine and chemokine expression in the small intestine of the indicated mice. **l**, Representative images of intestinal sections from 4-month-old mice with the indicated genotypes. Scale bars, 100 μm. $*P \leq 0.05$, $**P \leq 0.01$, $***P \leq 0.005$; NS, not significant.

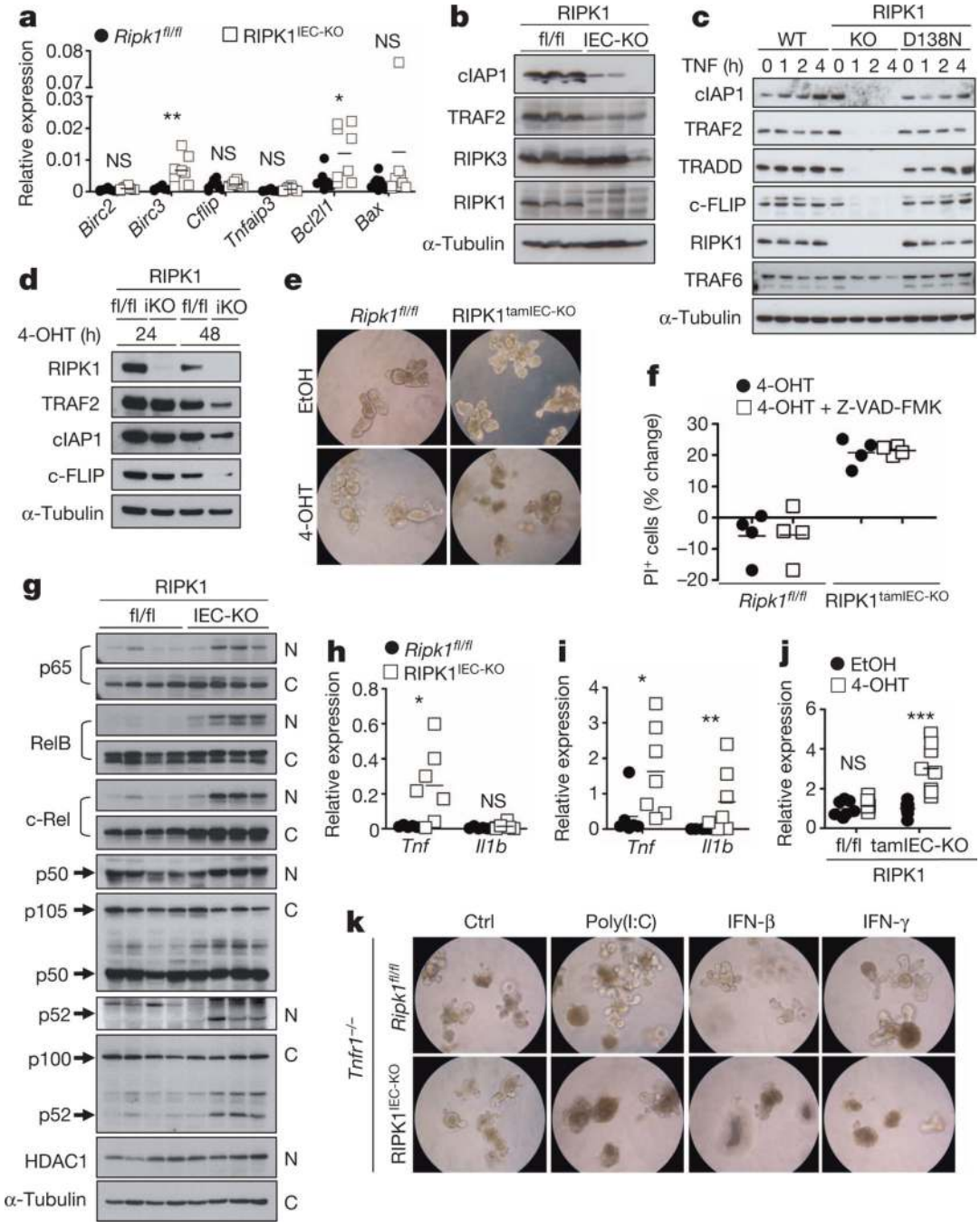

Figure 3. RIPK1 prevents the degradation of pro-survival proteins

a, **b**, qRT–PCR of pro-survival genes (**a**) and immunoblot of the indicated proteins (**b**) in small intestine IECs from *Ripk1*$^{fl/fl}$ (fl/fl) and RIPK1$^{IEC\text{-}KO}$ (IEC-KO) mice. **c**, Immunoblot of wild-type (WT), *Ripk1*$^{-/-}$ (KO) and *Ripk1*$^{D138N/D138N}$ (D138N) MEFs stimulated with 10 ng ml^{-1} recombinant murine TNF. **d**, Immunoblot of small intestine organoids from *Ripk1*$^{fl/fl}$ (fl/fl) and RIPK1$^{tamIEC\text{-}KO}$ (iKO) mice treated with 4-hydroxytamoxifen (4-OHT) for 24 or 48 h. **e**, *Ripk1*$^{fl/fl}$ and RIPK1$^{tamIEC\text{-}KO}$ organoids were treated with vehicle (ethanol; EtOH) or 4-OHT for 20 h and photographed 48 h later. Original magnification,

×400. **f**, FACS quantification of propidium iodide $(PI)^+$ cells in organoids 43 h after treatment with 4-OHT in the presence or absence of z-VAD-FMK. **g**, Immunoblot of cytoplasmic (C) and nuclear (N) proteins from small intestine IECs of four *Ripk1*$^{fl/fl}$ and four RIPK1$^{IEC\text{-}KO}$ mice with the indicated antibodies. **h**, **i**, qRT–PCR of *Tnf* and *Il1b* expression in IECs from small intestine (**h**) or colon (**i**) of *Ripk1*$^{fl/fl}$ and RIPK1$^{IEC\text{-}KO}$ mice. **j**, qRT–PCR of *Tnf* expression in small intestine organoids from *Ripk1*$^{fl/fl}$ and RIPK1$^{IEC\text{-}KO}$ mice 30 h after treatment with EtOH or 4-OHT. **k**, Representative images of *Ripk1*$^{fl/fl}$/*Tnfr1*$^{-/-}$ and RIPK1$^{IEC\text{-}KO}$/*Tnfr1*$^{-/-}$ organoids 16 h after treatment with 100 μg ml^{-1} poly(I:C), 1,000 U ml^{-1} IFN-β and 1,000 U ml^{-1} IFN-γ. Original magnification, ×400. Ctrl, control. Representative data are shown of four (**e**, **f**, **k**), three (**c**) or two (**d**, **j**) independent experiments. *P ≤0.05, **P ≤0.01, ***P ≤0.005; NS, not significant.

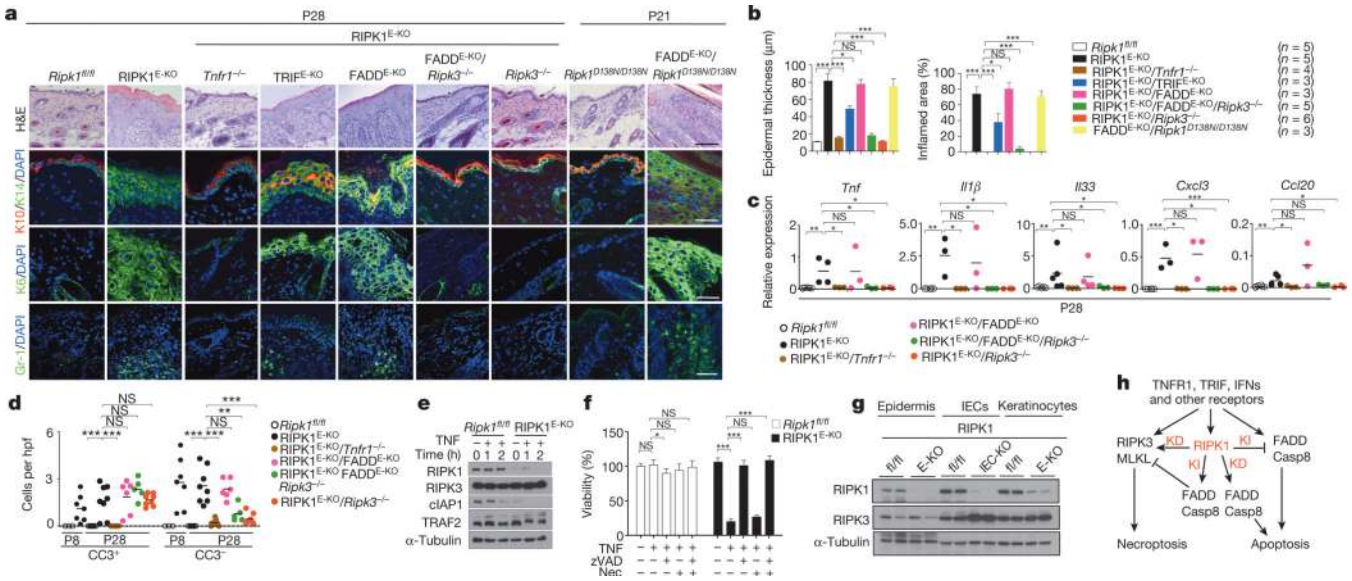

Figure 4. RIPK1 ablation causes keratinocyte necroptosis and skin inflammation

a, Representative images of skin sections from the indicated mice stained with H&E or the indicated antibodies. Nuclei stained with 4′,6-diamidino-2-phenylindole (DAPI). Scale bars, 100 μm (H&E); 50 μm (immunostainings). **b**, Microscopic quantification of epidermal thickness and inflamed skin area in the indicated mice. Error bars represent mean values ± standard error of the mean (s.e.m.). **c**, qRT–PCR of cytokine and chemokine expression in total skin from the indicated mice. **d**, Quantification of $CC3^+$ and $CC3^-$ dying cells per high power field (hpf) in skin sections from the indicated mice. **e**, Immunoblot of primary keratinocytes stimulated with 20 ng ml^{-1} recombinant murine TNF for the indicated time points. **f**, Quantification of cell viability in primary keratinocytes treated with 50 ng ml^{-1} recombinant murine TNF in the presence or absence of z-VAD-FMK (zVAD; 20 μM) and necrostatin-1 (Nec; 30 μM). Mean values ± s.e.m. from biological triplicates ($n = 3$) are shown. **g**, Immunoblot of protein extracts from P4 epidermis, IECs or keratinocytes from mice of the indicated genotypes. **h**, Schematic model of the kinase-dependent (KD) and -independent (KI) functions of RIPK1 in apoptosis and necroptosis. Representative data of three independent experiments are shown in **e**, **f**. $*P \leq 0.05$, $**P \leq 0.01$, $***P \leq 0.005$; NS, not significant.